

Comprehensive Investigation on Content-based Medical Image Retrieval Using Radon Barcodes

by

Syed Raazi Rizvi

A thesis submitted to the School of
Graduate and Postdoctoral Studies in
partial fulfillment of the requirements for
the degree of

Masters of Applied Science

in

Computer and Electrical Engineering

Ontario Tech University

Computer and Electrical Engineering

Oshawa, Ontario, Canada

December 2019

Copyright © Syed Raazi Rizvi, 2019

Thesis Examination Information

Thesis title: Comprehensive Investigation on Content-Based Medical Image Retrieval Using Radon Barcodes

An oral defense of this thesis took place on November 15, 2019 in front of the following examining committee:

Examining Committee:

Chair of Examining Committee	Dr. Ying Wang
Research Supervisor	Dr. Shahryar Rahnamayan
Research Co-Supervisor	Dr. Bekir Yilbas
Examining Committee Member	Dr. Masoud Makrehchi
External Examiner	Dr. Khalil El-Khatib

The above committee determined that the thesis is acceptable in form and content and that a satisfactory knowledge of the field covered by the thesis was demonstrated by the candidate during an oral examination. A signed copy of the Certificate of Approval is available from the School of Graduate and Postdoctoral Studies.

Abstract

Content Based Medical Image Retrieval (CBMIR) systems are vital to the underlying operation of medical databases because they allow quick search and retrieval of medical images. Radon Barcode (RBC)s are binary complementary feature vectors which increase the speed of CBMIR systems through smaller feature vector size and low retrieval error. We explore further improving the efficiency and accuracy of RBCs by optimizing the way they are extracted from medical images. Through the addition of image pre-processing, novel barcoding techniques, and improved distance evaluation methods, we improved RBC utility in CBMIR applications. Image pre-processing techniques such as histogram equalization and adaptive thresholding reduced the retrieval error of generated RBCs. We also introduce several novel barcode generation techniques such as Binary Coded Decimal Radon Barcodes (BCDRBC), Difference of Radon Projections Barcodes (DRPBC), and Difference of Radon Projections Soft Hash Barcode (DRPSHBC) which decreased both retrieval error and barcode size.

AUTHOR'S DECLARATION

I hereby declare that this thesis consists of original work of which I have authored. This is a true copy of the thesis, including any required final revisions, as accepted by my examiners.

I authorize the University of Ontario Institute of Technology to lend this thesis to other institutions or individuals for the purpose of scholarly research. I further authorize University of Ontario Institute of Technology to reproduce this thesis by photocopying or by other means, in total or in part, at the request of other institutions or individuals for the purpose of scholarly research. I understand that my thesis will be made electronically available to the public.

Syed Raazi Rizvi

STATEMENT OF CONTRIBUTION

The work described introduces three new Radon Barcode (RBC) generation techniques in Chapter 3; Binary Coded Decimal Radon Barcodes (BCDRBC), Difference of Radon Projections Barcodes (DRPBC), Difference of Radon Projections Soft Hash Barcode (DRPSHBC). In addition to quantitatively comparing the RBC introduced in [35] with all the improvements in Chapter 3 using the Image Cross Language Evaluation Forum (ImageCLEF) evaluation method on the Image Retrieval Medical Application (IRMA) dataset.

Acknowledgements

I want to convey my deepest gratitude to my research supervisor Dr. Rahnamayan whose support, mentorship, and guidance helped me throughout my education at the University of Ontario Institute of Technology. Additionally, I would like to acknowledge Dr. Tizhoosh, whose research in medical imaging served as the basis for this work. Finally, I must express my very profound gratitude to my parents and family for providing me with unfailing support and continuous encouragement throughout my years of study and through the process of researching and writing this thesis. This accomplishment would not have been possible without them.

Thank you.

Syed Raazi Rizvi

Contents

Abstract	ii
Acknowledgements	v
Contents	vi
List of Figures	viii
List of Tables	ix
Acronyms	ix
1 Introduction	1
1.1 Content Based Medical Image Retrieval	4
1.2 Thesis Objectives and Outline	7
2 Background	8
2.1 Image Pre-processing for CBMIR Systems	9
2.1.1 Histogram Equalization	10
2.1.2 Image Segmentation	12
2.2 The Radon Transform and Barcode	20
2.2.1 Radon Transform	20
2.2.2 Radon Barcode Formation	27
2.3 Barcodes and Medical Image Retrieval	29
2.3.1 Supervised Approaches to CBMIR	30
2.3.2 Supervised Approaches to CBMIR	31
3 Experimental Methodology	34
3.1 IRMA Dataset	34
3.1.1 ImageCLEF Challenge	35
3.1.2 CBMIR Performance Evaluation	36
3.2 Distance Measure	38

4	Experimental Results	41
4.1	Image Standardization	44
4.1.1	Histogram Equalization	44
4.1.2	Image Binarization	46
4.2	Radon Barcode Generation	49
4.2.1	Binary Coded Decimal Radon Barcodes	50
4.2.2	Difference of Radon Projections Barcodes	53
4.2.3	Soft Radon Hash Barcodes	55
4.3	Distance Measures	59
5	Conclusions and Future Work	60
5.1	Conclusions	60
5.2	Summary of Contributions	63
5.3	Future Research Direction	64
	Bibliography	65

List of Figures

1.1	CBMIR Framework	5
2.1	Effects of equalizing image histograms	11
2.2	Effect of adaptive thresholding on an input image	16
2.3	Z_n (3×3) kernel for computing image gradients	17
2.4	Prewitt Kernel	18
2.5	Sobel Kernel	19
2.6	Effect of edge binarization techniques on input image	19
2.7	CT Scanning Process	21
2.8	Radon Transform parameterization	23
2.9	Radon Barcode	27
3.1	Radon Barcode	35
3.2	Radon Barcode	37
3.3	Example Computing OTU	39
4.1	Feature Extraction in CBMIR systems	42
4.2	Soft Radon Hash	56
4.3	Segmentation of Pmiddle Region from the Radon Transform (RT) and the Gradient	56

List of Tables

2.1	Best results reported in literature for supervised RBC approaches . . .	31
2.2	Best results reported in literature for un-supervised RBC approaches	32
3.1	Sub-axes error score evaluation for the IRMA retrieval error	37
3.2	OTU Expression of Binary Instances i and j	39
4.1	Comparison between RBC results reported in [35] and those generated with our test environment	43
4.2	Effect of applying histogram equalization on retrieval accuracy, E_{total}	46
4.3	Effect of binarizing images with Adaptive thresholding on retrieval accuracy, (E_{total})	47
4.4	Effect of binarizing images with Prewitt edge detection on retrieval accuracy, (E_{total})	48
4.5	Effect of binarizing images with Sobel edge detection on retrieval accuracy, (E_{total})	48
4.6	Effect of binarizing images with Canny edge detection on retrieval accuracy, (E_{total})	49
4.7	Effect of binarization of input images with edge filters and thresholding on retrieval accuracy, (E_{total})	49
4.8	RBC and BCDRBC retrieval accuracy (E_{total})	52
4.9	RBC and DRPBC retrieval accuracy (E_{total})	54
4.10	RBC and RSHDRPBC retrieval accuracy (E_{total})	58
4.11	Effect of different distance measures, HD and BED on RBC retrieval accuracy (E_{total})	59

Acronyms

BCD	Binary Coded Decimal.
BCDRBC	Binary Coded Decimal Radon Barcodes.
BED	Binary Euclidean Distance.

CAD	Computer-Aided Diagnosis.
CBIR	Content Based Image Retrieval.
CBMIR	Content Based Medical Image Retrieval.
CNN	Convolutional Neural Network.
CNNC	Convolutional Neural Network Codes.
CT	Computed Tomography.
DICOM	Digital Imaging and Communications In Medicine.
DRPBC	Difference of Radon Projections Barcodes.
GBC	Gabor Barcode.
GC	Gray Code.
GRBC	Radon-Gabor Barcodes.
HD	Hamming Distance.
ImageCLEF	Image Cross Language Evaluation Forum.
IR	Image Retrieval.
IRMA	Image Retrieval Medical Application.
KNN	K Nearest Neighbors.
LBP	Local Binary Patterns.
LRD	Local Radon Descriptor.
OTU	Operational Taxonomic Units.
PACS	Picture Archiving and Communication Systems.
RASH	Radon Soft Hash.
RBC	Radon Barcode.
ROI	Region of Interest.
RT	Radon Transform.
SVM	Support Vector Machine.

Chapter 1

Introduction

Advances in the areas of digital imaging, computer hardware, and information storage have caused a generation of massive amounts of multimedia content. Within the past few decades, digital images have become one of the most popular types of media content, and the proliferation of imaging devices suggests that this trend will only continue to grow. Modern image databases store images by organizing and indexing image data for efficient content search, manipulation, and retrieval. Storing digital images requires abstraction of data into a data structure which is compatible with conventional database operations (i.e., insert, delete, and search). Intelligently organizing and searching image data requires the creation of a meta-heuristic distance metric often called a similarity measure, which differentiates images into different clusters or classes.

A similarity measure is a distance measure between two sets of characteristic features which compare either semantic information or distinctive features of a query image to others stored within a database. Each stored image contained within the database structure is assigned an index, mapping its location in memory along with

its representative feature vector. Effective similarity measures are difficult to create because they contain a large amount of information which is multi-dimensional (i.e., multiple classes in the same image).

Image Retrieval (IR) techniques search and retrieve images from image databases based on text-based similarity measures derived from text labels, descriptions, annotations, and etc. Image Retrieval (IR) systems rely on creating descriptive text labels/tags in hopes that they accurately describe image content, and then organize image data using standard document retrieval techniques. Problems with scalability and complexity arise when practically implementing IR systems. Each image stored into a IR database needs to be manually tagged, described, or annotated with representative text by a human annotator. Annotation is usually performed without any contextual reference (i.e., cat vs. pet), often leading to problems with consistency and or bias. Retrieval accuracy in IR systems is questionable at best because images often belong to more than one category and can be misclassified by annotators. A common obstacle which all IR approaches face, is that manual image annotation/label generation puts practical limitations on system scalability. Although automation of the text label generation/annotation process seems like the logical solution, it would require a system to translate image content into textual information correctly, a problem which has yet to be solved. Stopping short of automatic text annotation, Content Based Image Retrieval (CBIR) can provide similar functionality to IR systems without practical limitations in scalability and accuracy.

Content Based Image Retrieval (CBIR) systems, introduced in the early 90's and gradually saw widespread integration into all major social and media platforms, automating image search and retrieval tasks. Instead of relying on keywords, image

meta-data, or surrounding text; CBIR approaches construct a feature vector from image pixel data using computer vision and image processing techniques. Feature vectors are then compared quantitatively to find their level of similarity or conversely, the difference between images. Image data contained in a CBIR compatible database automatically has its similarity to the entire database measured when first stored. CBIR systems are the next step in automating database search and retrieval technologies and have already seen widespread use in different industries such as Medicine, Intellectual Property, Broadcast Media, and Internet Search because of their versatility and flexibility [41].

In CBIR systems there are four primary factors affecting system design; feature extraction and representation, dimensionality reduction, indexing, and query handling [41]. Out of the four factors, feature extraction and representation is the most critical in order to extract and represent various types of image content. Image features are created from patterns of color, shape, and textures contained within an image, and are used to determine the distance between a query image and all other images contained within a CBIR database. Engineering these image features can be a challenging task as there are two competing objectives; retrieval accuracy, and feature size. Feature accuracy is the measure of how well extracted visual feature(s) represents an image, and how well they can classify objects contained within the image. Memory size is a significant factor in feature engineering, because it has a direct impact on the retrieval time and the overall usability of the CBIR system.

1.1 Content Based Medical Image Retrieval

The medical industry, in particular, relies heavily on Content Based Image Retrieval (CBIR) systems to power Computer-Aided Diagnosis (CAD). Patient record information is often incomplete and difficult to obtain due to time and privacy restrictions. Studies show that diagnosis by trained medical professionals based solely on medical images isn't always consistent and can vary significantly [7]. One of the significant sources causing such inconsistencies is lack of reliable data on symptoms, medical and family history, etc. Picture Archiving and Communication Systems (PACS) is a health informatics standard which integrates different imaging modalities, patient history/records and interfaces them with hospital information systems. Picture Archiving and Communication Systems (PACS) also manages the storage and dissemination of medical images to a variety of individual and corporate subscribers [41]. A critical component of PACS is its CBMIR system which allows it to search its medical image databases efficiently. Another benefit of PACS is that it allows individuals or corporate entities to glean patient information in multiple modalities from a single source. CBMIR systems allow PACS to index, search, and retrieve medical image data because they are not reliant on textual data and can already process existing records contained within image databases. Using CBMIR systems also allows medical professionals to trace similar historical cases based on the similarity of their medical images, allowing for the development of better diagnostic models and protocols. The advancement of such systems is critical to the development of data-based diagnostic techniques which potentially provides life-saving information to medical professionals.

CBMIR systems share a common framework with conventional CBIR approaches as shown in Figure 1.1. When initially, an medical image database is created, and the

by reducing the size of the representative image feature vector to a manageable size, and using specialized filters to extract only the most salient features. However, in medical imaging, the size and resolution of the images vary based on the type of image device and method used. Practically this translates to creation longer feature vectors, which in turn are computationally more expensive to process. Exasperating the challenges mentioned above is the fact that misclassification in CBMIR systems can lead to potentially fatal consequences (i.e., misdiagnosis).

One solution which is used to combat the problem of large and computationally expensive feature vectors is to use complementary feature vectors to pre-search CBMIR image databases. Binary codes such as the Radon Barcode (RBC) ([35]) have been proposed complementary feature vectors, because of their small feature vector size and their relatively simple generation methods. RBCs have high retrieval error rates which affect their viability as complementary feature vectors for CBMIR applications.

Some the key challenges in implementing RBC as complementary feature vectors are that they encode very little information about the image itself, so it is critical to capture unique defining characteristics of the medical image being barcoded. In this study we found several ways to filter medical images to remove noise and other non-unique visual features through image processing. We suggested several key improvements to the RBC generation process by introducing three new barcoding techniques as well finding an optimal binary distance metric for barcode comparison. A key contribution of this work is that it quantitatively compares the RBC introduced in [35] with all suggested improvement using the Image Cross Language Evaluation Forum (ImageCLEF) evaluation method on the IRMA dataset. This study and the proposed methods are novel in the area of RBC research because the introduced bar-

coding methods are global in nature and a comparative analysis provided between the proposed approaches and the initial RBC investigation.

1.2 Thesis Objectives and Outline

The primary objective of this work was to reduce the retrieval error of Radon Barcode (RBC)s for Content Based Medical Image Retrieval (CBMIR) applications. A secondary objective was to reduce barcode length so RBCs require fewer computational resources. We explored novel optimizations and improvements to the RBC techniques which reduce retrieval error and barcode length. Validating our results with the Image Cross Language Evaluation Forum (ImageCLEF) evaluation method on the Image Retrieval Medical Application (IRMA) dataset allowed us to test the efficacy of our proposed optimizations. Understanding the type of images being bar-coded, the barcode generation and comparison process was critical to improving RBC retrieval error and reducing barcode length.

This investigation focused on the impact which image pre-processing, new barcode generation, and barcode evaluation techniques had on reducing CBMIR retrieval error and barcode length. Chapter 1 introduced complementary feature vectors and their usage in CBMIR systems. Chapter 2 provided readers with a background on the RT, image processing, RBC generation, and an overview of current RBC approaches found in literature. Chapter 3 explained the procedure used to evaluate complementary feature vectors such as the RBC in CBMIR systems. Chapter 4 discussed the proposed image pre-processing, barcoding generation, and distance evaluation techniques using the methodology introduced in Chapter 3. Chapter 5 briefly discusses our conclusions, contributions, and outlines future research directions.

Chapter 2

Background

Content Based Medical Image Retrieval (CBMIR) is a rapidly developing field and has been one of the most promising applications of Content Based Image Retrieval (CBIR) systems to date. One advantage of modern health-care facilities is that they collect massive quantities of image data, because of the sheer volume of patients which they have processed. Unfortunately, significant portions of the collected data are left underutilized because of scalability, privacy, and or integration restrictions/roadblocks. CBMIR systems present a potential solution to the issues of privacy and scalability, because they can automatically search through millions of medical image to find a list of relevant hits to a search query with minimal human involvement. It is important to note that CBMIR systems are software based systems and suffer from the same risks and privacy concerns associated with any such system. In the past a critical limitation of medical image retrieval systems has been maintaining patient privacy because image data needed to be heavily controlled and restricted. CBMIR systems have helped overcome these roadblocks by using computer algorithms to review medical images instead of human evaluators, and are generally agnostic to a patients identity. Another critical limitation of traditional medical image retrieval

systems is that clinicians often don't have time to compare their patients medical images against databases and had to rely on their own past experiences. Diagnostic information ascertained from medical imaging is reasonably consistent when reviewed by software algorithms and can be used as a baseline similarity metric to assist when searching for related medical information such as symptoms and treatment plans etc. CBMIR systems save time and money, arming clinicians with a powerful tool at their fingertips, automating what used to be very time-consuming and resource-intensive task.

2.1 Image Pre-processing for CBMIR Systems

In order to effectively extract representative feature vectors from medical images, Content Based Medical Image Retrieval (CBMIR) systems, must first apply image processing techniques to normalize and standardize the medical image data. Comparing two medical images has been an inherently difficult task, because images are often captured using different imaging devices and under individual conditions. Therefore, it was critical to standardize and normalize all the images stored within medical image databases to minimize the noise and variability which may be passed on to the feature extraction phase. Picture Archiving and Communication Systems (PACS) specifies a recommended image processing procedure which should be implemented by imaging equipment before storing within a medical image database [4]. The primary image pre-processing stages outlined in the PACS standard are histogram modification, artifact/background removal, and orientation correction. Histogram modification techniques serve the dual purpose of filtering out any noise contained within an medical image and normalizing medical images to one standardized histogram range. In ra-

diation imaging, background refers to anywhere outside of the radiation field which in turn shows up as white in resulting image (often referred to as a collimator). The removal of this background region is necessary because it affects histogram based approaches in either extracting features or further enhancing the image. Medical images, when captured are not always in a standard orientation and vary due to practical limitations in equipment and imaging procedures. Differences in image orientation can translate to errors when finding the similarity of two images; thus it is critical to detect and correct the direction of medical images when storing them into a database. The techniques mentioned above are some of the most basic and widely used pre-processing steps when processing medical images, so it is not surprising that modern CBMIR systems employ some or all of the aforementioned techniques.

2.1.1 Histogram Equalization

One of the most widely used histogram modification techniques in medical imaging is histogram equalization. For any given gray scale image pixels are sorted into k discrete bins using Equation 2.1 [31] [15]. In Equation 2.1 L represents original gray scale intensities, s_k is the new calculated intensity level, n_j is the number pixels which have an intensity level equal to that of j , and MN are the number of pixels in the input image.

$$s_k = \text{floor} \left(\frac{(L-1)}{MN} \sum_{j=0}^k n_j \right) \quad (2.1)$$

Content Based Medical Image Retrieval (CBMIR) systems often use histogram equalization as a pre-processing stage prior to feature extraction, because the technique increases image contrast potentially leading to improved feature extraction.

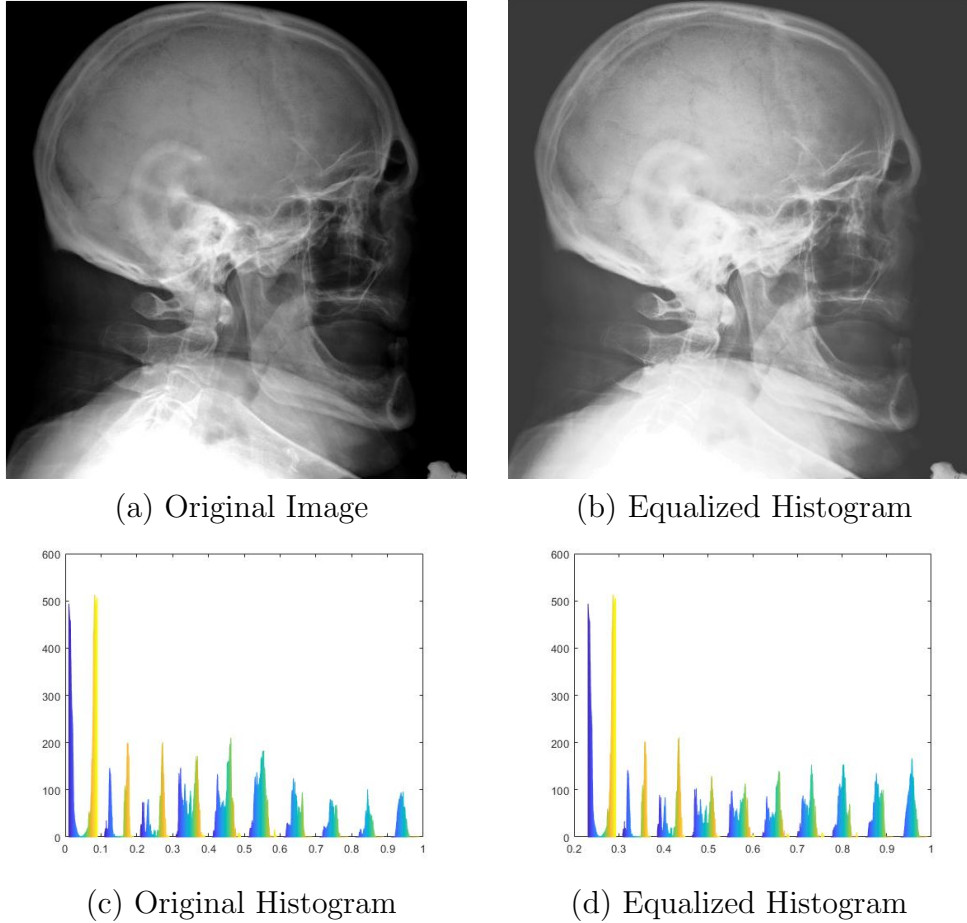


Figure 2.1: Effects of equalizing image histograms

Figure 2.1(a) shows an medical image prior to histogram equalization and (c) shows the its histogram. Figure 2.1(b) shows the same image with its histogram equalized (d). Comparing 2.1 (a) and (b), greater detail can be seen from image (b) rather than image (a). Looking at the histograms, 2.1 (c) and (d), the effect of equalization can be seen as (d) has a much flatter distribution than (c). Additionally it is important to note that by equalizing the histogram we reduce intensity variations from the image capture device(s). Histogram equalization is a valuable pre-processing stage for medical images being used with CBMIR systems because it can potentially increase the amount and quality of the extracted features.

2.1.2 Image Segmentation

Removing artifacts and abnormalities in medical images sometimes requires filtering digital images with binary masks which subtract/filter out unnecessary data such as background, or artifacts (i.e., implants, jewelry, etc..). Alternatively, masks may be applied to highlight or segment out regions of interests within the image, such as bone, tumors, and etc. Segmentation techniques primarily rely on a two-phase approach: First isolating regions of interests such as area of specific intensity, shape, or structure. Second classifying identified regions of interest to see if they fit known classes. Isolating regions of interest is critical in Content Based Medical Image Retrieval (CBMIR) applications, because the ability to store only targeted features directly affects a systems retrieval speed and thus usability. Medical image segmentation usually is fairly simple; A gray scale image is converted to a binary image usually based on some intensity threshold or structural element. Once a medical image is converted into a binary representation it must undergo further filtering/segmentation to find a target region of interest or feature which can be used to classify the image. Segmentation improves performance and potentially retrieval accuracy in CBMIR systems by removing unwanted features/noise and encoding targeted features/patterns within a smaller feature vector.

Image Thresholding

Thresholding is an image segmentation approach which classifies image pixels based on their intensity or color. Each pixel is classified from a binary comparison between the image color/intensity and some calculated value. Pixel classification can be performed with a simpler globally or more accurate locally determined threshold. The information required to represent images can be reduced by storing its color/intensity

data as a multi-modal distribution based on a classification criterion. Content Based Medical Image Retrieval (CBMIR) systems usually involve some form of thresholding to reduce feature vector size and to help isolate key features to be encoded.

One of the most popular thresholding methods was proposed by Otsu in [26], which assumes that an image contains two distinct classes (bi-modal distribution), and uses discriminant analysis to exhaustively search for the optimal threshold to minimize intraclass variance, σ_{ω}^2 (Equation 2.2), by maximizing the interclass variance, σ_b^2 (Equation 2.4). Where t is the current threshold, L is the total number of intensity levels, ω_0, ω_1 are the class weights, $\omega_0(t), \omega_1(t)$ are the class probabilities, $\sigma_0^2(t), \sigma_1^2(t)$ are the class variances, $\mu_0(t), \mu_1(t)$ are the class means, μ_T is mean for the image, and $p(i)$ is the number of pixels for each intensity level.

$$\text{Intraclass variance: } \sigma_{\omega}^2(t) = \omega_0(t)\sigma_0^2(t) + \omega_1(t)\sigma_1^2(t) \quad (2.2)$$

$$\text{Interclass variance: } \sigma_{\omega}^2(t) = \omega_0(\mu_0 - \mu_T) + \omega_1(\mu_1 - \mu_T) \quad (2.3)$$

$$\sigma_b^2(t) = \omega_0(t)\omega_1(t)[\mu_0(t) - \mu_1(t)]^2 \quad (2.4)$$

where,

$$\text{Class 0 probability: } \omega_0(t) = \sum_{i=0}^{t-1} p(i) \quad (2.5)$$

$$\text{Class 1 probability: } \omega_1(t) = \sum_{i=t}^{L-1} p(i) \quad (2.6)$$

$$\text{Class 1 mean: } \mu_0(t) = \frac{\sum_{i=0}^{t-1} ip(i)}{\omega_0(t)} \quad (2.7)$$

$$\text{Class 2 mean: } \mu_1(t) = \frac{\sum_{i=t}^{L-1} ip(i)}{\omega_1(t)} \quad (2.8)$$

$$\text{Histogram mean: } \mu_T = \sum_{i=0}^{L-1} ip(i) \quad (2.9)$$

Equation 2.2 gives the relationship between intraclass variance and the two weighted distributions (bi-modal case) in terms of threshold value, where smaller variances correspond to better thresholds. Conversely the optimal threshold can also be determined from finding maximum interclass variance (Equation 2.4), because at that threshold value both class distributions are the most separable. Class 0 and 1 probabilities can be found by summing the probability of pixels occurring in all the intensity levels starting from 0 and going up to the current threshold, t . Similarly class 1 probabilities are found by summing the probability of occurrence for pixels in intensity levels starting from the current threshold, t , and going up to the maximum intensity value for the image, L . Class means for classes 0 and 1 are calculated by summing the products of intensity level with the probability of pixel occurrence (for each class range $[0 \dots t]$ or $[t \dots L]$) and re-normalizing the results to overall class probabilities. Calculating the histogram mean simply involves finding the product of all the intensity levels found in the image with their probability of occurrence. Maximizing σ_b (Equation 2.4) increases distance between the two class distributions, and gives us the optimal threshold for classification. Otsu's proposed approach is a quick and efficient manner to determine the optimal intensity threshold for bi-modal images.

Adaptive thresholding proposed by Bradley and Roth [6] is another popular method which is both robust and takes into account changes in illumination which often occur in images. This approach also utilizes integral images [40], which enable the rapid

calculation of local intensity sums, thereby improve processing times for localized thresholding. Integral images, are defined by Equations 2.10- 2.11, where $f(x, y)$ is the original image and $I(x, y)$ the Integral Image. Equation 2.10 shows how to calculate an integral image; where $I(x, y)$ is the summation of all intensity values in the rectangular region above and to the left of pixel (x, y) . Whereas Equation 2.11 shows the calculation of local sum in the rectangular region $(x1, y1)$ and $(x2, y2)$ Bradley and Roth proposed to use an SxS neighborhood average to binarize individual pixels between intervals based on their percentage difference to each other.

$$I(x, y) = f(x, y) + I(x - 1, y) + I(x, y - 1) - I(x - 1, y - 1) \quad (2.10)$$

$$\textit{Where} : x = 1 \dots M, y = 1 \dots N, I(0, 1) = I(1, 0) = I(0, 0) = 0,$$

$$M = \text{Number of rows in } f(x, y), N = \text{Number of columns in } f(x, y).$$

$$\sum_{x=x1}^{x2} \sum_{y=y1}^{y2} f(x, y) = I(x2, y2) - I(x2, y1 - 1) - I(x1 - 1, y2) + I(x1 - 1, y1 - 1) \quad (2.11)$$

Using Otsu's global threshold in place of a neighborhood average in Bradley and Roths adaptive thresholding technique, we obtain an optimal thresholding method which proves quite useful for identifying regions of interest within medical images as shown in Figure 2.2

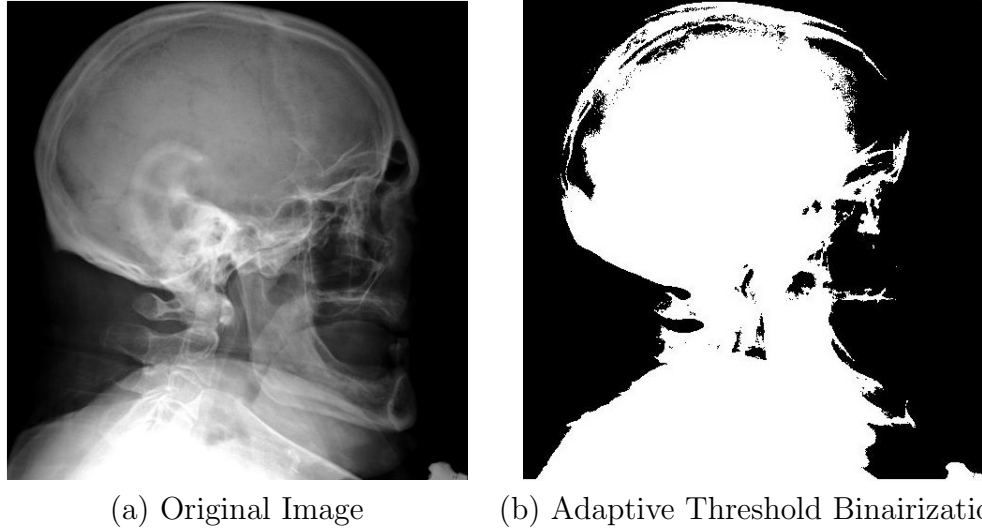


Figure 2.2: Effect of adaptive thresholding on an input image

Image Edge Detection

Edge detection is the determination of object boundaries within an image, and can be found through many different methods, many of which convolve every image pixel with a kernel comprised of its local neighborhood pixels. Supervised Content Based Medical Image Retrieval (CBMIR) systems sometimes use edge detection techniques remove unwanted image regions (i.e. implants, collimator) which may introduce bias into the feature vector. Unsupervised CBMIR systems sometimes encode feature vectors extracted from edge-images (images which have undergone edge detection) to significantly reduce feature vector size, albeit with lower accuracy.

Most standard edge detection techniques such as the ones proposed by Prewitt, and Sobel ([27], [32]) use a (3×3) operator kernel to calculate the image gradient (Figure 2.3). Operator kernels are weighted to emphasize the changes from top/bottom rows and left/right columns to find the partial derivatives (G_x, G_y) to approximate the image gradient. Processing images with operator kernels first requires centering

the kernel onto the image pixel currently being processed ($z_5 = I(x, y)$), and multiplying the overlapped regions of the kernel with the corresponding pixel intensities. Partial derivatives of the image are calculated using Equations 2.15-2.16 to approximate the x and y components of the image gradient (G_x, G_y). Figure 2.3 shows the mapping between 3×3 operator kernel (Z_n) and the partial derivatives (G_x, G_y) used to calculate the image gradient. The approximated partial derivatives (G_{xy}, G_y) for the image are used to calculate the image gradient (G_{xy}) using Equation 2.14. After the image gradient is calculated, a threshold value (I_{Thresh}), similar to Equation 2.12 found using the mean value ($\overline{G_{x,y}}$) and size (n) of the 3×3 operator kernel. Threshold, (I_{Thresh}), is then used to binarize the image locally, creating a mask of vertical and horizontal edges contained within the image (edge-image).

$$I_{Thresh} = \sqrt{n \cdot \overline{G_{x,y}}} \quad (2.12)$$

$$\nabla f = \begin{bmatrix} G_x \\ G_y \end{bmatrix} = \begin{bmatrix} \frac{\delta f}{\delta x} \\ \frac{\delta f}{\delta y} \end{bmatrix} \quad (2.13)$$

$$G = \sqrt{G_x^2 + G_y^2} \quad (2.14)$$

z_1	z_2	z_3
z_4	z_5	z_6
z_7	z_8	z_9

Figure 2.3: Z_n (3×3) kernel for computing image gradients

Prewitt edge detection, uses only the vertical and horizontal components of the image gradient (∇f) to find gradient of the image intensity of gray-scale images. Equations 2.15 and 2.16 show the approximation of the partial derivatives in Prewitt

edge detection, and Figure. 2.4 shows to the 3×3 Prewitt operator kernels which are convolved with the image to approximate the image gradient.

Sobel edge detection is another edge detection technique which builds up on the Prewitt operator but has a more pronounced spectral response because of increased weight on the horizontal (x) and vertical sections (y) of the operator ([1]). As Equations 2.17 and 2.18 show the $z_2, z_4, z_6,$ and z_8 pixels of the operator kernel have double the weight in comparison to other pixels (see Figure 2.5). This amplifies the image gradient (∇f) in the $N, W, E,$ and S directions thus helping the Sobel operator kernel detect straight edges better than the Prewitt's. A more comprehensive explanation and comparison of the two edge detection techniques can be found in ([32], [11], [27]).

$$G_x = (z_7 + z_8 + z_9) - (z_1 + z_2 + z_3) \quad (2.15)$$

$$G_y = (z_3 + z_6 + z_9) - (z_1 + z_4 + z_7) \quad (2.16)$$

-1	-1	-1	-1	0	1
0	0	0	0	-1	1
1	1	1	1	-1	1
G_x			G_y		

Figure 2.4: Prewitt Kernel

$$G_x = (z_7 + 2 \cdot z_8 + z_9) - (z_1 + 2 \cdot z_2 + z_3) \quad (2.17)$$

$$G_y = (z_3 + 2 \cdot z_6 + z_9) - (z_1 + 2 \cdot z_4 + z_7) \quad (2.18)$$

Advanced edge detection approaches such as Canny's technique ([8], [9], [16])

-1	-2	-1
0	0	0
1	2	1

$$G_x$$

-1	0	1
-2	0	2
-1	0	1

$$G_y$$

Figure 2.5: Sobel Kernel

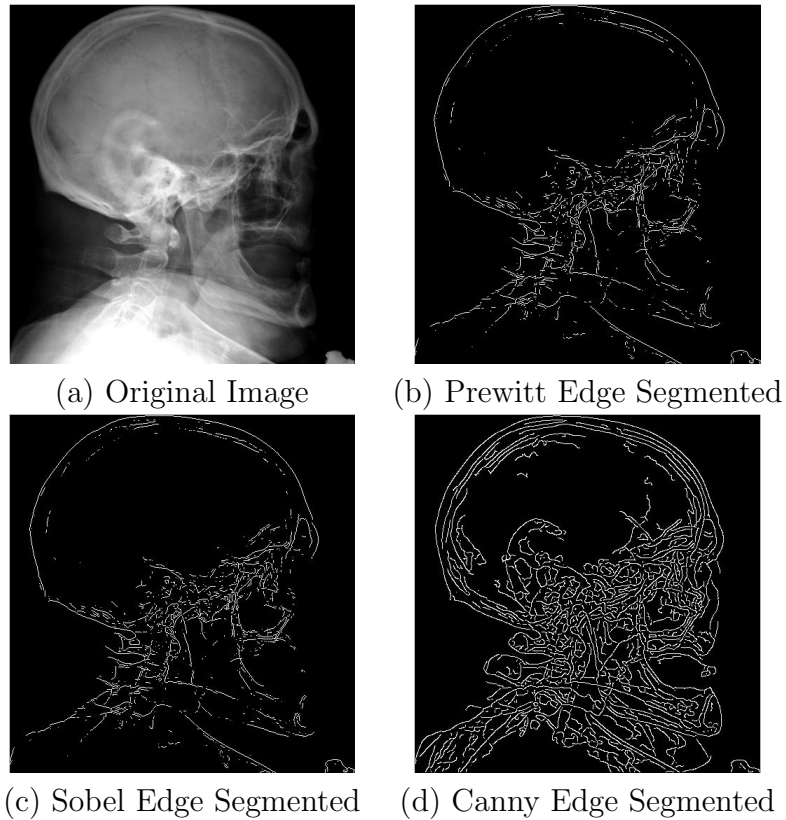


Figure 2.6: Effect of edge binarization techniques on input image

first smoothen the image intensity with Gaussian filters prior to edge detection with conventional operator (Sobel, Prewitt) in order increase the amount of information captured in the edge-image. Figure 2.6 shows the detected edges from a medical image using the three edge detection techniques (Prewitt, Sobel, and Canny) discussed in this section. Differences between the Prewitt and Sobel edge detectors (Figure 2.6 (b)-(c)) operators appear to be barely noticeable, because the image has few straight or horizontal boundaries. In this case the outputs from both Prewitt

and Sobel edge detection techniques will be nearly identical because the additional weight for N, S, E, W directions in the Sobel operator kernel is mitigated by the lack of changes between image pixels in said directions. Edge detection from the Canny technique (Figure 2.6 (d)) captures more information than the Prewitt or Sobel operators, because it smoothens the image prior to edge detection. However not all the additional edges captured are useful, because the majority of the additional information is caused by small intensity variations which have been introduced due to the smoothing/filtering the original image.

Motivation for the application of edge detection techniques in CBMIR systems mainly stems from the removal of unwanted objects in supervised approaches and for the creation of smaller feature vectors from binary images instead of gray-scale ones. The effects of edge detection techniques on unsupervised CBMIR systems is further explored in Section 4.1.2 for the creation of feature vectors for image retrieval systems. For a more detailed explanation of the application of edge detection techniques and methodologies readers are directed to [22] [16] [11].

2.2 The Radon Transform and Barcode

2.2.1 Radon Transform

Medical imaging has one primary purpose; to assess the state of internal body anatomy or pathology. Imaging biological systems within the body is a very challenging task because patients have many different biological/anatomical systems within a minimum imaging depth or region. Additionally taking medical images requires bombarding a patient with radiation (X-rays, alpha particles, etc. . .) which can be detrimental

to patients health. Within medical imaging, X-rays are one of the most common imaging modality because of their high accessibility and relatively low cost. X-ray images show both hard and soft tissues as the images are a negative of the X-ray intensity reported from the detector/collector. Hard masses such as bones and tumors absorb low energy radiation preventing it from passing through the body to the detector directly behind, whereas soft tissues allow radiation to pass straight through. Imaging methods such as X-rays are referred to as projection techniques because the detector is placed directly behind the target and the absence of radiation measured. A more comprehensive explanation of X-ray imaging techniques is found in [28].

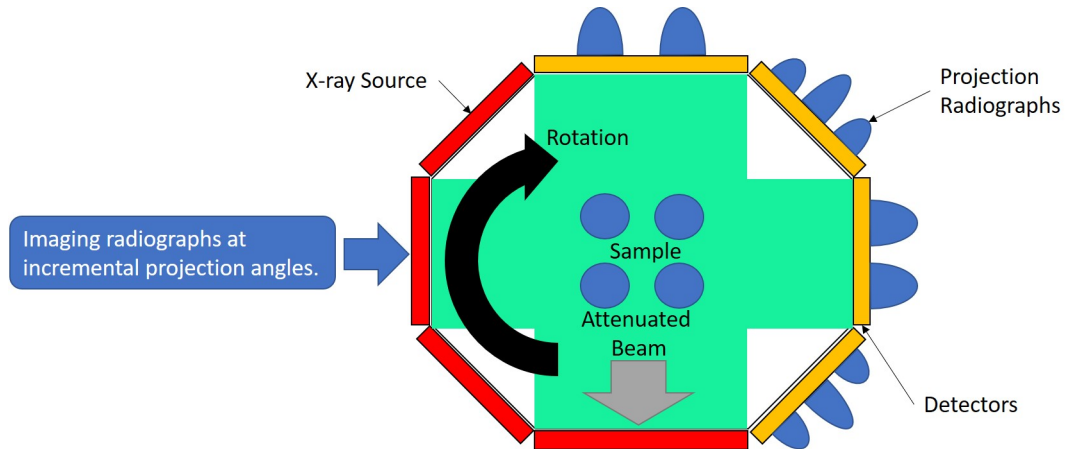


Figure 2.7: Computed Tomography (CT) imaging process.

A more comprehensive imaging technique is Computed Tomography (CT) scanning which uses a revolving X-ray source and detector such as shown in Figure 2.7. X-ray sources and corresponding detectors are fixed to a rotating platform to collect projection intensity profiles at different angles. Mathematical reconstruction techniques such as the Radon Transform (RT) are used to reconstruct these projections. In 1917, Johann Radon published his work "On the determination of functions from integrals along certain manifolds.". Johann's work provided a mathematical founda-

tion for Cormack and Hounsfield technique on reconstructing cross-sectional images using X-ray radio-graphs [12]. The forward RT is found by taking any straight line, ρ , which passes through an object $f(x, y)$ and the x-y plane origin and calculating the projection of $f(x, y)$ onto it. Formally the RT of function, $f(x, y)$, can be defined as the integral along a line L (perpendicular to ρ) as shown in Equation 2.19.

We can parameterize x and y in terms of a plane formed by two lines which intersect the origin of object $f(x, y)$, S and ρ , as shown in Eq. 2.21-2.22. Substituting Eq. 2.21 and Eq. 2.22 into Eq. 2.19 we obtain Eq. 2.23 which represents the projection or the RT of object $f(x, y)$ onto line ρ at angle ϕ . Parameterizing x and y in terms of a linear combination of ρ and S allows for a simpler and more intuitive representation of the RT, as shown in Figure 2.8. It is also possible to convert back from the RT with the Inverse Radon Transform (IRT) to reconstruct projections of object $f(x, y)$ at all available angles ϕ back into an gray-scale image, a more detailed explanation on this process is found in [12].

$$\hat{f}(\rho, \phi) = R\{f(x, y)\} = \int_L f(x, y) ds \quad (2.19)$$

$$\rho = x \cos \phi + y \sin \phi \quad (2.20)$$

$$x = \rho \cos \phi - s \sin \phi \quad (2.21)$$

$$y = \rho \sin \phi + s \cos \phi \quad (2.22)$$

$$\hat{f}(\rho, \phi) = \int_{-\infty}^{\infty} f(\rho \cos \phi - s \sin \phi, \rho \sin \phi + s \cos \phi) ds \quad (2.23)$$

Computation of the RT in all subsequent sections of this work was performed using the approach outlined in [5], and is described below. The distribution of image

Processing digital images with the RT first requires converting an image to gray-scale, choosing the projection angles (θ), finding the image min/max (N, M), finding the image origin (O_{xy}), determining the maximum projection size (j), and initializing the radon output matrix (\mathbf{p}). Digital x-ray images are usually stored gray-scale format and sometimes need to be normalized with the techniques described in image pre-processing steps as described in Section 2.1 done to find a better RT. To find the maximum projection size (j), the length between image origin (O_{xy}) and the maximum image height (y) and width (x) are calculated ($Size_{P_{\frac{xy}{2}}}$). Double the value of this length ($Size_{P_{\frac{xy}{2}}}$) represents the maximum amount of pixels (j) which can be projected onto line ρ at any given angle (θ_i). Initializing the output radon projection matrix is done by initializing a matrix of zeros (\mathbf{p}) with a length of the maximum projection size (j) and a width equal to the maximum number of projection angles (K).

Calculating the RT begins first with selecting the set of angles, θ , over which the transform will be calculated. Typically, this set of angles (θ) is an input parameter for the RT and projections of $I(x, y)$ onto line ρ are calculated at each angle (θ_i) iteratively and stored in the output matrix of the RT transform (\mathbf{p}). To find the projections onto line ρ begins with calculating the Cosine and Sine tables, which are used to transform image I from $x - y$ to $\rho - \theta$ space at 0.5 pixel intervals. To calculate the Cosine and Sine tables, the pixel column (n)/row (m) are converted into x/y values by subtracting the x and y components of the image origin (O_x/O_y). The Cosine and Sine tables for the image ($xCosTable, ySinTable$) are calculated by finding the cos and sine values of the projection angle currently being processed (θ_i), and multiplying it with the values for x/y with a $+/-0.25$ offset (to achieve a 0.5 interval). After the Cosine and Sine tables are calculated the projection of the neighboring pixels

Algorithm 2.2 Algorithm to Compute Radon Transform (RT)

```
1: Initialize the gray-scale image to be transformed,  $I(x, y) \leftarrow f(x, y)$ 
2: Initialize  $k$  projection angles for the transform,  $\boldsymbol{\theta} \leftarrow \theta_0, \theta_1, \dots, \theta_K$ 
3: Initialize the maximum x size of the image I,  $N \leftarrow \max_x(I(x, y))$ 
4: Initialize the maximum y size of the image I,  $M \leftarrow \max_y(I(x, y))$ 
5: Initialize the origin of image  $I(x, y)$ ,  $O_x \leftarrow \frac{N-1}{2}, O_y \leftarrow \frac{M-1}{2}$ 
6: Find the maximum projection size:  $Size_{P_{\frac{y}{2}}} \leftarrow M - 1 - O_y, Size_{P_{\frac{x}{2}}} \leftarrow N - 1 - O_x,$   

 $Size_{P_{\frac{xy}{2}}} \leftarrow \text{ceil}(\text{Sqrt}(Size_{P_{\frac{y}{2}}}^2 + Size_{P_{\frac{x}{2}}}^2 + 1)), j = 2 * Size_{P_{\frac{xy}{2}}} + 1$ 
7: Initialize the output radon projection matrix,  $\mathbf{p} \leftarrow \text{zeros}(j, k)$ 
8: for  $i \leftarrow 0 : k$  do
9:   for  $n = 0 : N$  do
10:      $x = n - O_x$ 
11:      $x\text{CosTable}[2 * n] = (x - 0.25) * \cos(\theta_i)$ 
12:      $x\text{CosTable}[2 * n + 1] = (x + 0.25) * \cos(\theta_i)$ 
13:   end for
14:   for  $m = 0 : M$  do
15:      $y = m - O_y$ 
16:      $y\text{SinTable}[2 * m] = (y - 0.25) * \sin(\theta_i)$ 
17:      $y\text{SinTable}[2 * m + 1] = (y + 0.25) * \sin(\theta_i)$ 
18:   end for
19:   for  $n = 0 : N$  do
20:     for  $m = 0 : M$  do
21:        $x = n - O_x$ 
22:        $y = m - O_y$ 
23:       if  $pixel \neq 0$  then
24:          $pixel = 0.25 * I(x, y)$ 
25:          $r \leftarrow x\text{CosTable}[2 * n] + y\text{SinTable}[2 * m] - Size_{P_{\frac{xy}{2}}}$ 
26:          $\text{IncrementRadonProjection}(pixel, \mathbf{p}_r, \theta_i, r)$ 
27:          $r \leftarrow x\text{CosTable}[2 * n + 1] + y\text{SinTable}[2 * m] - Size_{P_{\frac{xy}{2}}}$ 
28:          $\text{IncrementRadonProjection}(pixel, \mathbf{p}_r, \theta_i, r)$ 
29:          $r \leftarrow x\text{CosTable}[2 * n] + y\text{SinTable}[2 * m + 1] - Size_{P_{\frac{xy}{2}}}$ 
30:          $\text{IncrementRadonProjection}(pixel, \mathbf{p}_r, \theta_i, r)$ 
31:          $r \leftarrow x\text{CosTable}[2 * n + 1] + y\text{SinTable}[2 * m + 1] - Size_{P_{\frac{xy}{2}}}$ 
32:          $\text{IncrementRadonProjection}(pixel, \mathbf{p}_r, \theta_i, r)$ 
33:       end if
34:     end for
35:   end for
36: end for
37: end
38: Return  $\mathbf{p}$ 
```

of (x, y) onto line ρ are tabulated and incremented into the output matrix (p_{r,θ_i}) at a point r along the ρ axis. This is done by first finding the pixel being processed in the $x - y$ plane by subtracting the image origin $O_{x,y}$ from the pixel column (n) and row (m) to find the (x, y) coordinates in terms of pixel column and row indices. The gray-scale intensity value at the pixel coordinates (x, y) is then divided by four (0.25) to account for the superposition of four neighborhood pixel projections (NE, NW, SE, SW). The point r in line ρ for each x, y coordinate is found by using Eq. 2.20 and subtracting half the maximum projection distance ($SizeP_{\frac{x,y}{2}}$) to prevent sub-region overlap.

Projections of the intensity values for four neighborhood pixels (NE, NW, SE, SW) are then superimposed onto the output matrix (\mathbf{p}) using Alg. 2.1. To find the projection of image pixel located at coordinate (x, y) onto line ρ at point r several temporary variables such as pixel intensity ($pixel1$), location along ρ ($r1$), and a small variance ($delta$) are initialized. Incrementing the output projection matrix is achieved by tabulating the summation of pixel intensity ($pixel1$) at coordinate (x, y) multiplied by a smoothing factor of $(1 - delta)$ with the current projection value $(\mathbf{p}_{r1,\theta_i})$. Additionally a tiny component of the pixel intensity value ($pixel1 * delta$) being processed is added to the next point r in the output matrix $(\mathbf{p}_{r1+1,\theta_i})$ for smoothing the output. This superposition happens for all four neighborhood pixels (NE, NW, SE, SW) and provides a good approximation for the intensity projection of coordinate (x, y) onto the line ρ at point r . This process is repeated for each non-zero intensity pixel in the image currently being transformed, giving us the radon transform of the image ($I(x, y)$) at angle currently being processed (θ_i)

2.2.2 Radon Barcode Formation

Radon Barcode (RBC) have been shown to be a useful feature vectors for unsupervised Content Based Medical Image Retrieval (CBMIR) systems. First proposed in [35], they have steadily gained popularity and slowly become more accurate. Using binary codes is an increasingly common trend in CBMIR systems because they are, integrated easily within current medical systems and barcodes are easy to interpret (provided the barcoding scheme). Barcodes such as RBCs, offer a much smaller vector length comparable to traditional approaches (i.e., templates, text, and some categorical) and they are much more transparent in their generation process. RBCs show significant promise for use in CBMIR applications due to their traceability and performance benefits.

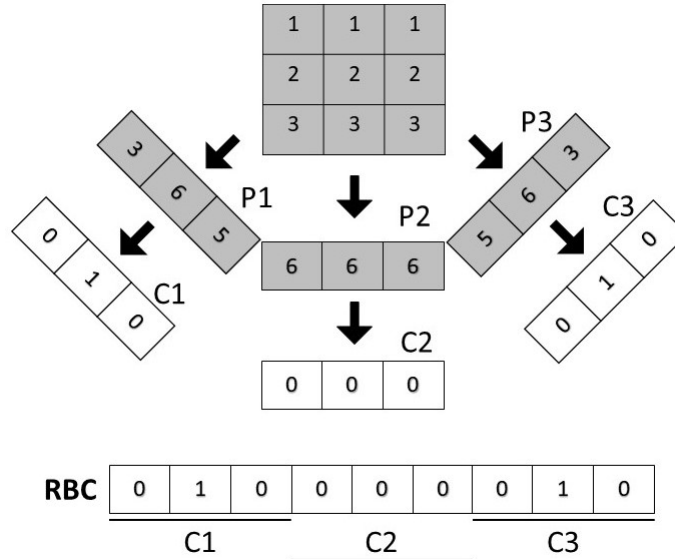


Figure 2.9: RBC formation

The RBC generation process is shown graphically in Figure 2.9 and denoted in Algorithm 2.3. Barcode generation begins with first rescaling a gray-scale medical image (i.e., X-Ray image) to an arbitrary square size (e.g., 32*32). After which we

Algorithm 2.3 Radon Barcode Algorithm (RBC)

- 1: Initialize Radon Barcode $r \leftarrow \emptyset$
 - 2: Initialize angle $\theta \leftarrow 0$ and $R_N = C_N \leftarrow 32$
 - 3: Normalize the input image $\bar{I} = \text{Normalize}(I, R_N, C_N)$
 - 4: Set the number of projection angles, e.g. $n_p \leftarrow 4$
 - 5: **while** $\theta < 180$ **do**
 - 6: Get all projections \mathbf{p} for θ
 - 7: Find typical values: $T_{\text{typical}} \leftarrow \text{median}_i(\mathbf{p}_i)|_{p_i \neq 0}$
 - 8: Threshold projections: $\mathbf{b} \leftarrow \mathbf{p} \geq T_{\text{typical}}$
 - 9: Append the new row $\mathbf{r} \leftarrow \text{append}(\mathbf{r}, \mathbf{b})$
 - 10: $\theta \leftarrow \theta + \frac{180}{n_p}$
 - 11: **end while**
 - 12: **end**
 - 13: Return \mathbf{r}
-

find the Radon transform for np projections (where $\theta = 0, \dots, 180$) to extract the barcode. Each selected Radon projection has its median value or typical value (T_{typical}) calculated for all non-zero elements. Using the typical value T_{typical} as threshold each selected radon projection vector is then binarized. The RBC is finally created by concatenating the np binary vectors into a single row vector.

Variants of the RBC approach adopt a similar barcoding processing and generally follow a three-stage generation process derived from the original method. First, the images are normalized, scaled, and have other pre-processing stages applied to them, including possible binarization of the original image. Since the radon transform is an integral transform, it is valid both continuous and discrete cases (refer to [12]). Barcodes for localized regions of an image although more accurate, require extensive investigations into optimal Region of Interest (ROI) selection for each dataset and are therefore excluded from this investigation. The second stage is to apply some transformation to the radon projections and then formulate a single barcode which represents binary encoded image features. For cases where the resulting barcode con-

tains real integer values, they are rescaled to the range of 0-256, stored as unsigned 8-bit integers (UINT8), and encoded using Gray Code (GC) [14]. The final stage compares the generated barcode to the database using a quantitative measure of similarity/difference as discussed in the next section.

2.3 Barcodes and Medical Image Retrieval

Medical images are usually stored using Digital Imaging and Communications In Medicine (DICOM) which is a standardized format for storing and retrieving medical images from centralized databases. Digital Imaging and Communications In Medicine (DICOM) files not only contain digital photos, but relevant meta-data required for interpreting the stored image such as patient history, image device information, and etc. Most major imaging equipment manufacturers output raw image data in conjunction with relevant imaging parameters/configurations which allow experts to determine the accuracy and utility of the image for their specific application (i.e., an X-ray image of the chest may represent a single image, or be a slice of a CT scan). Content Based Medical Image Retrieval (CBMIR) systems use the meta-data provided in the DICOM format to find relationships and links between database entries to organize image data in specific groups or classes. Search, and retrieval methods typically involve some combination of supervised learning techniques with unsupervised image processing methods to achieve optimal results.

H. Tizhoosh presented one such unsupervised approach [35], which used Radon Barcode (RBC) extracted from DICOM images in order to serve as possible secondary similarity measure for CBMIR systems. The approach created short binary codes from

the Radon transform of X-ray images, which were orders of magnitude smaller in size compared to visual features and outperformed current binary codes (namely Local Binary Patterns (LBP)). Many other subsequent research studies inspired by RBC developed new techniques for implementing and training CBMIR systems using similar methodologies. The studies can be broken down into two categories, supervised (Table 2.1) and un-supervised (Table 2.2), and subsequently ranked based on their best results in 2.1-2.2 (based on the ImageCLEF Image Retrieval Medical Application (IRMA) error see Chapter 3.1.2).

2.3.1 Supervised Approaches to CBMIR

Supervised approaches use one or more machine learning techniques to accurately learn classes which they use for the search and retrieval phase of Content Based Medical Image Retrieval (CBMIR) systems. Liu et. al. proposed Convolutional Neural Network Codes (CNNC) [21] which are a combination of Radon Barcode (RBC) with traditional Convolutional Neural Network (CNN). The authors suggest shortlisting candidate solutions with a Convolutional Neural Network (CNN) and using RBC to determine the distance between short-listed results. After testing their approach on the Image Retrieval Medical Application (IRMA) dataset they were able to achieve a much better accuracy than the initially RBC approach in [35]. Zhu et al., proposed a CBMIR system [42] which used Support Vector Machine (SVM), K Nearest Neighbors (KNN), and RBC. Their approach used RBC codes generated from X-ray images to train a multi-class Support Vector Machine (SVM) classifier, which then were clustered and retrieved using K Nearest Neighbors (KNN). Erfankhah et al. proposed training multi-class SVMs with Radon-Gabor Barcodes (GRBC) [13], which are extracted from Radon transformed images. Inspired by the RBC technique researchers

also used deep auto-encoding and transfer learning techniques ([34], [37], [17]) to find optimal binary representations of the Radon transform. Most promising of which, Khatami et al. [17], proposes using the difference between two orthogonal Radon projections within the selection pooling phase of transfer learning model to create a salient Local Binary Patterns (LBP) code.

Table 2.1: Best results reported in literature for supervised RBC approaches

Approach	E_{total}^{best}
[21]	224.13
[42]	294.83
[34]	344.08
[37]	392.09
[17]	168.05
[33]	313.17
[13]	248.03

2.3.2 Supervised Approaches to CBMIR

Unsupervised techniques mainly focus on improving the underlying image processing techniques/methods to better improve retrieval accuracy in supervisory systems. However, unsupervised approaches can also be applied independently of any learning based technique, albeit with lower accuracy. This characteristic proves to be important in cases where training data is scarce and not readily available, or in computationally constrained systems. In [35] Radon Barcode (RBC)s were presented by H. Tizhoosh as a supplementary similarity measure to assist improve retrieval time in Content Based Medical Image Retrieval (CBMIR) systems. Tizhoosh et al. also proposed encoding only the transition between local maxima and minima of each Radon projection to improve retrieval accuracy [39]. Nouredanesh et al. also pro-

posed two methods for creating barcodes using Gabor filters and RBC [24]. The first method Gabor Barcode (GBC) [24] creates binary codes from the output of a Gabor filter bank in a similar fashion to [35], improving overall search accuracy, but with increased barcode length. In their second approach, they generate Radon-Gabor Barcodes (GRBC) [25], which are Gabor Barcode (GBC) of the Radon transform of an image as compared to the digital image itself. Babaie et al. proposed using an exploitation search scheme [3] using a Radon projection created by the approaches in [35] and [39] to create small selection pool of candidate images which then are used drastically improve search accuracy while keeping a small barcode size. Babaie et. al. proposed Local Radon Descriptor (LRD) [2] which utilize orthogonal radon projection pairs to create a local descriptor for image content which encodes localized image information as compared to a global approach (RBC).

Table 2.2: Best results reported in literature for un-supervised RBC approaches

Approach	E_{total}^{best}
[35]	470.57
[39]	447.04
[2]	287.77
[24]	351.80
[25]	322.41

In [38], Tizhoosh and Rhanamayan explored the possibility of finding the optimal number of projections to represent each image to yield a higher retrieval accuracy using the evolutionary techniques presented in [29]. RBCs also have been applied in other application areas such as tumor ROI segmentation [36] to provide a fast localization scheme for detecting tumors within ultrasound images. The amount of recent research into the application of RBC approaches both supervised and unsupervised shows the development of new and exciting research area in the field of binary code

generation for medical image retrieval, which will have a profound impact on medical image retrieval industry. The development of such techniques is critical to the practical implementation and deployment of CBMIR systems within the medical devices and systems.

Chapter 3

Experimental Methodology

In the previous chapter, we introduced several investigations into the application of barcodes to Content Based Medical Image Retrieval (CBMIR) systems. A survey on Computer-Aided Diagnosis (CAD) [30] stated that any such system needs to be searchable in real-time, usable by physicians, and be able to show the logic behind its decisions. Unsupervised, CBMIR approaches are attractive in this respect, because a human can logically and quantitatively understand precisely why the algorithm arrived at a particular result or retrieved a specific image. CBMIR systems which use short binary codes prove practical and easily implementable real-world cases offering advantages in speed and performance. The approaches investigated in this work focus upon developing an accurate, traceable, and practically implementable technique for generating feature vectors for use in CBMIR systems.

3.1 IRMA Dataset

Studies mentioned in Chapter 2 were compared based upon their performance retrieving images from the X-ray image dataset, Image Retrieval Medical Application

(IRMA) [20]. Image retrieval from the IRMA dataset subsequently became a part of the Image Cross Language Evaluation Forum (ImageCLEF) challenge [23] which provided researchers with a quantitative means for ranking their proposed Content Based Medical Image Retrieval (CBMIR) approaches.

3.1.1 ImageCLEF Challenge

The Image Retrieval Medical Application (IRMA) dataset contains 12,677 labeled X-ray images for training, and 1733 images for validation. X-Ray images were collected and provided by the RWTH University Hospital of Aachen, Germany. Images were randomly collection from the daily routine work of the radiology department. The dataset contains significant variations in content, viewing angle, ages, gender, and quality. All images were rescaled to fit in a 512x512 bounding box while maintaining a fixed aspect ratio and stored using 256 gray levels (8-bits).

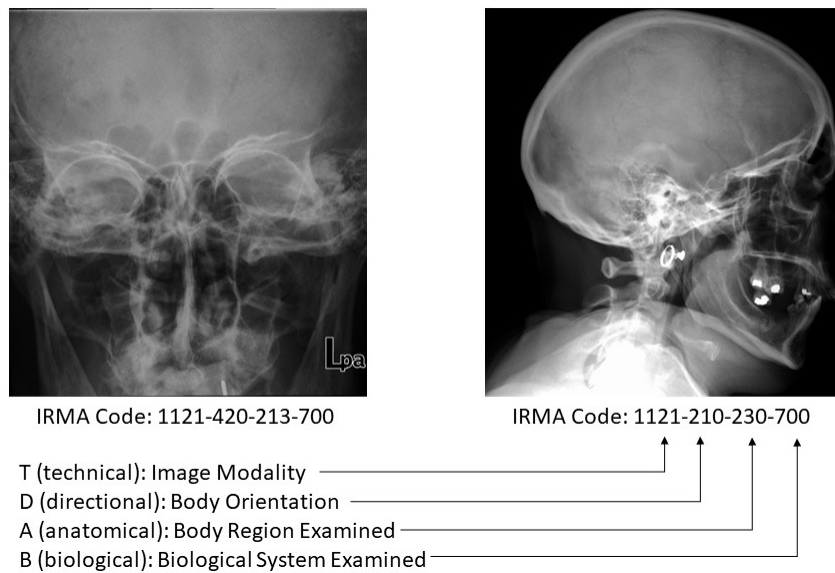


Figure 3.1: Description of 13 digit IRMA code for two X-Ray images

Each image is annotated by physicians with a code, TTTT-DDD-AAA-BBB, com-

prising of 13 characters depicting its four mono-hierarchical axes (see Figure 3.2): a four-digit technical code (T) representing image modality, a 3 digit directional code (D) depicting body orientation during the scan, a 3 digit anatomical code (A) showing which body region the scan represents, and a 3 digit biological code (B) outlining the bio-system being examined. All code sub-axes contain either a 3 or 4 characters ranging from $\{0, \dots, 9, a, \dots, z\}$, where '0' represents 'unspecified' and signifies a termination of sub-code (T,D,A,B). In all the IRMA dataset contains 169 unique codes for the test set and 193 for the training set. Furthermore, both the test and training sets contain an imbalanced number of images per code to simulate real-world situations.

3.1.2 CBMIR Performance Evaluation

Many proposed Content Based Medical Image Retrieval (CBMIR) approaches have used the Image Retrieval Medical Application (IRMA) database to validate their systems against. Image Cross Language Evaluation Forum (ImageCLEF) developed an performance metric to measure the image retrieval error for the IRMA dataset. CBMIR systems first generate a 13 character IRMA code for all the 1733 images contained within the test dataset. Each code compares against a ground truth value, and the error tabulated using Equation 3.1. Section (a) of Equation 3.1 accounts for the probability of the correct character occurring at i (branching factor). Section (b) accounts for the level difficulty in predicting true characters further into the code hierarchy (position in the string). Section (c) is the classification from CBMIR similarity measure determining if a query image matches the samples from the stored database. In Equations 3.1 and 3.2 $\hat{l}_{l_j,i}^m$ represents the query or reference image, $l_{l_j,i}^m$ represents the database image currently being compared, and $\delta(l_{l_j,i}^m, \hat{l}_{l_j,i}^m)$ the repre-

sents the binary code match.

$$E_{total} = \sum_{m=1}^{1733} \sum_{j=1}^4 \sum_{i=1}^{l_j} \underbrace{\frac{1}{b_{l_j,i}}}_a \underbrace{\frac{1}{j}}_b \underbrace{\delta(l_{l_j,i}^m, \hat{l}_{l_j,i}^m)}_c \quad (3.1)$$

where,

$$\delta(l_i, \hat{l}_i) = \begin{cases} 0 & \text{if } l_{l_j,i}^m = \hat{l}_{l_j,i}^m, \forall j \leq i \\ 1 & \text{if } l_{l_j,i}^m \neq \hat{l}_{l_j,i}^m, \exists j \leq i \end{cases} \quad (3.2)$$

classified	error count
463	0.000000
46*	0.025531
461	0.051061
4*1	0.069297
4**	0.069297
47*	0.138594
473	0.138594
477	0.138594
***	0.125000
731	0.250000

Table 3.1: Sub-axes error score evaluation for the IRMA retrieval error

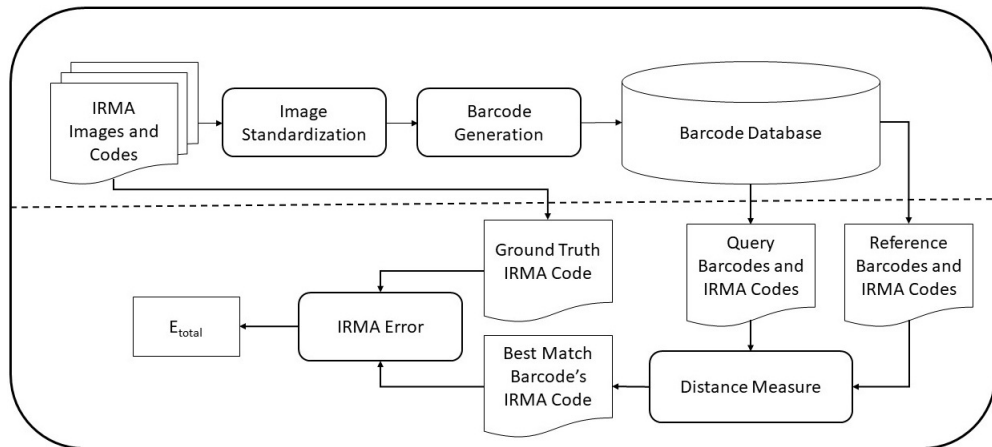


Figure 3.2: Graphical illustration of process to calculate E_{total}

After tabulating the error from IRMA codes, we find that it is possible to get a maximum error of 0.25 for a single axis and a minimum error score of 0. Table 3.1 shows several example code axes with their tabulated error values and Figure 3.2 illustrates the tabulation process. The IRMA error function is a means of effectively evaluating and comparing the retrieval accuracy of CBMIR systems. In the following chapter, proposed methodologies will be evaluated and compared using this error metric to determine the effectiveness of a technique in retrieving X-ray images

3.2 Distance Measure

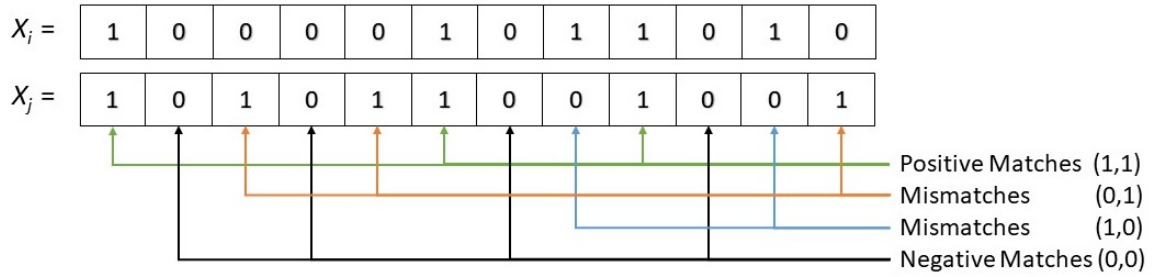
Comparing images to one another using binary vectors, although economical, does pose several challenges. First and foremost is the fact that binarizing information usually requires some encoding scheme or a thresholding method to reduce the dimensionality of the data contained therein. However, effectively finding an optimal dimensionality reduction technique is an ongoing effort, as there is no single approach which is best for all applications. Compounding to this problem is that each dimensionality reduction technique needs an appropriate similarity and distance metric which works best for that application. Choi et al. surveyed 76 binary similarity and distance measures [10] which have been used for hierarchical clustering in recent works and defined them according to their Operational Taxonomic Units (OTU).

Suppose that two images are represented by the binary vectors i and j ; let n be the dimension of the vector, a the number of positively matched elements in both vectors ($i = j = 1$), b the number of mismatched elements in vector i ($i = 0 \neq j = 1$), c the number of mismatched elements in vector j ($i = 1 \neq j = 0$), and d the number of negatively matched elements in both vectors ($i = j = 0$). Then we can define

different distance metrics in simple formulations using the mapping shown in Table 3.2 and Figure 3.3.

$j \backslash i$	1 (Presence)	0 (Absence)	Sum
1 (Presence)	$a = i \cdot j$	$b = \bar{i} \cdot j$	$a + b$
0 (Absence)	$c = i \cdot \bar{j}$	$d = \bar{i} \cdot \bar{j}$	$c + d$
Sum	$a + c$	$b + d$	$n = a + b + c + d$

Table 3.2: OTU Expression of Binary Instances i and j



		X_i		
		1	0	
X_j	1	$a = 3$	$b = 3$	$a + b = 6$
	0	$c = 2$	$d = 4$	$c + d = 6$
		$a + c = 5$	$b + d = 7$	$a + b + c + d = 12$

Postive Matches (a) = 3
 Negative Matches (b) = 4
 Matches (a+d) = 7
 Mismatches (b+c) = 5
 Total number of attributes (a+b+c+d) = 12

Figure 3.3: Example of how to compute OTU for two barcodes

$$D_{BinaryEuclidean} = \sqrt{b + c} = \sqrt{\sum b \oplus c} \quad (3.3)$$

$$D_{Hamming} = b + c = \sum b \oplus c \quad (3.4)$$

There are two well-established measures explicitly used for calculating the distance between binary vectors. These methods are the Binary Euclidean Distance (BED) and Hamming Distance (HD) as shown in Equations 3.3-3.4 defined in terms of Operational Taxonomic Units (OTU). More practically the term $b + c$ contained within each equation can be readily found between two binary vectors of the same size by applying an exclusive OR (\oplus) operation and summing the resultant vector. In all the subsequent experiments and analysis finding binary matches between two barcodes will be based on the results of applying Binary Euclidean Distance (BED) or Hamming Distance (HD), and matches determined by the lowest distance between the query and reference barcode.

Chapter 4

Experimental Results

In this section, we propose several novel optimizations to help improve the effectiveness of Radon Barcode (RBC)s as a complementary feature vector in Content Based Medical Image Retrieval (CBMIR) systems. Complementary feature vectors such as RBCs are used narrow down the search space, thereby improving retrieval performance and accuracy. We focus on enhancing the RBC through improvements in image pre-processing and by proposing several novel barcoding techniques (see Figure 4.1).

Selecting what barcoding or image processing steps to apply when generating RBC is an important decision because it could add or remove unique visual features from the medical image. We proposed applying histogram equalization or image binarization because they are commonly applied steps in Picture Archiving and Communication Systems (PACS) systems [41] which tended to improve retrieval accuracy while maintaining barcode length. We introduced three new barcoding techniques as improvements to the conventional RBC generation process. The Binary Coded Decimal Radon Barcodes (BCDRBC) which improves retrieval accuracy but increases barcode

length, Difference of Radon Projections Barcodes (DRPBC) which improves retrieval accuracy but maintains barcode length, or Difference of Radon Projections Soft Hash Barcode (DRPSHBC) which improves retrieval accuracy and reduces barcode length. In our investigations we also found the optimal binary code similarity measure to be the Binary Euclidean Distance (BED), because it tended to increase retrieval error.

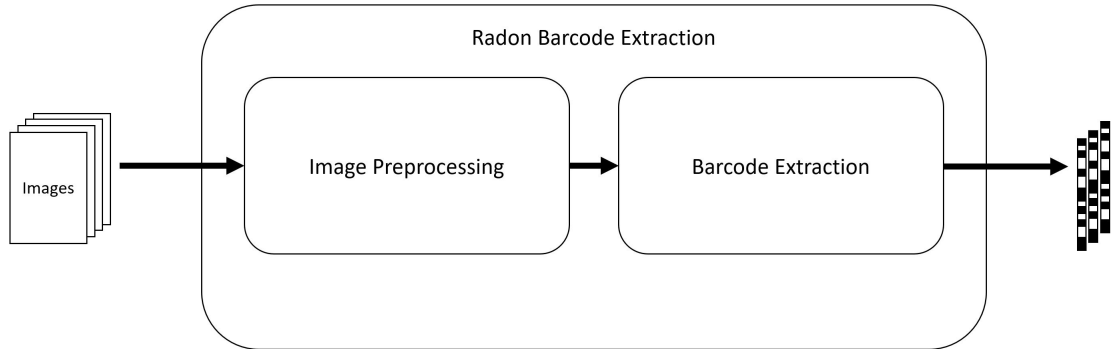


Figure 4.1: Feature Extraction in CBMIR systems

The results presented in this section have been generated with the Image Retrieval Medical Application (IRMA) dataset and evaluated with the Image Cross Language Evaluation Forum (ImageCLEF) evaluation technique introduced in Section 3.1.2. Experiments were conducted on a machine with Intel Core-I7 @ 2.7 GHz, 16 GB RAM, and Matlab 2017b used as the development/testing environment. To compare the effectiveness of our optimizations to the RBC technique we re-generated the E_{total} and L_{code} for the values reported in [35] with the Matlab 2017b Radon Transform (RT) function (see Algorithm 2.2). RBCs were generated from the IRMA dataset using Algorithm 2.3, and the retrieval error (E_{Total}) was calculated using Equation 3.1 in accordance with the ImageCLEF competition guidelines. Hamming Distance (HD) (Equation 3.4) was used as the distance metric to find the reference IRMA code (\hat{l}^m) for the binary match decision in Equation 3.2. The branching factor ($b_{i,j}$) (Section

3.1.2), was dynamically calculated for each digit based upon the IRMA code hierarchy. Results from the comparison between the two testing environments in Table 4.1 for 4, 8, 16, and 32 projection angles shown.

n_p	Reported		Regenerated	
	L_{code}	E_{total}	L_{code}	E_{total}
4	512	476.62	196	514.76
8	1024	478.54	392	477.34
16	2048	470.57	784	466.89
32	4096	475.92	1568	456.34

Table 4.1: Comparison between RBC results reported in [35] and those generated with our test environment

When comparing the image retrieval results generated between the two testing environments; Matlab 2017b and Matlab 2013b, we found that there were significant differences in RBC barcode length. Differences in barcode length between the reported and generated results were the result of the RT function dynamically calculating the maximum projection output size (j). Matlab versions after 2013b use Algorithm 2.2 to calculate the RT which doesn't pad the projection vectors with zeros, and instead calculates j for each image. Dependencies between the retrieval error of the regenerated results and those reported in [35] were caused by dynamically calculating the branching factor in Equation 3.1(a) for each digit in the IRMA code hierarchy. The initial investigation ([35]) fixed the branching factor to 10 with the assumption that each digit can only have 10 possible values ((0, ..., 9)); Artificially increasing the retrieval error because codes in the IRMA dataset are actually alphanumeric ((0, ..., 9, a, ..., z)). We compare all subsequent experiments to the reproduced results shown in Table 4.1 to determine retrieval accuracy for each proposed barcoding technique.

As is shown in Table 4.1 using the newer Matlab 2017b function for calculating the RT and dynamically determining the branching factor leads to a slightly better RBC retrieval error and smaller barcode lengths. Additionally, to observe the effect of each technique individually and do not chain methods/optimizations in our experiments. Individual testing is performed to isolate the effects of each proposed method and because they can affect downstream processes.

4.1 Image Standardization

Medical images, as stated in Section 2.1 contain noise and artifacts which need to be filtered out before any feature extraction can take place. Two typical pre-processing methods for medical images are; (a) Removing the collimator background, (b) and correcting the image orientation by applying rotation transforms. Fortunately, the images contained within the Image Retrieval Medical Application (IRMA) dataset already have been pre-processed so that there are minimal collimator artifacts and stored in the correct (upright) orientation. To further enhance the X-ray images before feature extraction, we normalize and resize images to a standard size and re-scale the intensity values between 0 and 1. We tested the two image pre-processing techniques, histogram equalization, and edge detection on their potential to help decrease the overall image retrieval error (E_{Total}) for the IRMA dataset.

4.1.1 Histogram Equalization

As noted in Section 2.1.1 the most common histogram modification technique for Content Based Medical Image Retrieval (CBMIR) systems is equalization, which flattens

out an otherwise skewed distribution within X-ray images. In this sub-section, we apply the histogram equalization technique which were introduced in Section 2.1.1 to Image Retrieval Medical Application (IRMA) dataset images before they are used to generate RBCs (Algorithm 2.3). Equalizing image histograms mitigates the effect of skewed image intensity distributions resulting from the X-ray imaging device used, illumination conditions, and different subjects. The results for this experiment are shown in Table 4.2 compared with the regenerated retrieval error (E_{Total}) and barcode size (L_{code}). Applying histogram equalization before Radon Barcode (RBC) generation reduced the average retrieval error by 21.27 or 4.5%. Redistribution of the image histogram for all the images in the IRMA dataset could explain the reduction in retrieval error. X-ray images in the IRMA dataset were captured using multiple imaging devices, illumination conditions, and patients. Equalizing image histograms before the Radon transform and RBC generation could have reduced intensity variations between visually similar images. The effect of reducing the intensity variations would have made similar RBCs spatially closer to each other, and resulted in smaller retrieval errors. When testing the effects of histogram equalization with the IRMA dataset, we found that increasing the number of projection angles (n_p) did not correspond to a decrease in retrieval error. As shown in Table 4.2, the most significant reduction in retrieval error occurs when the RBC went from being generated using four to eight projection angles, which corresponded to a decrease in retrieval error of 7.6%. In table 4.2 we see that the RBC of images pre-processed with histogram equalization had the lowest retrieval error with 32 projection angles ($n_p = 32$). Pre-processing images before RBC generation reduces the impact of intensity variations caused in X-ray images because of varying medical devices, illumination conditions, and tissue density.

	$RBC_{Regenerated}$		$RBC_{Hist.Eq.}$	
n_p	L_{code}	E_{total}	L_{code}	E_{total}
4	196	514.76	196	494.74
8	392	477.34	392	457.13
16	784	466.89	784	442.34
32	1568	456.34	1568	436.05

Table 4.2: Effect of applying histogram equalization on retrieval accuracy, E_{total}

4.1.2 Image Binarization

Babaie et al. reported in [3] that the Radon Barcode (RBC) barcoding process is highly sensitive to bright/dark areas often found in X-ray images. After testing with the image thresholding and edge detection techniques described in Section 2.1.2, we observed similar findings. Binarizing X-ray images from the Image Retrieval Medical Application (IRMA) dataset, before generating RBCs had a mixed effect on retrieval error (E_{total}) as shown in Table 4.7.

Adaptive thresholding (see Section 2.1.2) of X-ray images prior to RBC generation reduced the retrieval error, as shown in Table 4.3. Pre-processing the images with adaptive thresholding improved RBC retrieval error by removing small intensity variations caused by varying densities within each patients body (see Figure 2.2), through binarization. Table 4.3 shows that adaptive thresholding did not affect the RBC barcode length. However, the retrieval error decreased as the number of projection angles increased, albeit with diminishing returns. RBCs from images pre-processed with adaptive thresholding contained more representative information about the patient body shape/structure thus reducing retrieval error.

When the Prewitt, Sobel, and Canny edge detection techniques were used to filter

	$RBC_{Regenerated}$		$RBC_{Adap.Thresh}$	
n_p	L_{code}	E_{total}	L_{code}	E_{total}
4	196	514.76	196	486.49
8	392	477.34	392	457.97
16	784	466.89	784	441.84
32	1568	456.34	1568	443.22

Table 4.3: Effect of binarizing images with Adaptive thresholding on retrieval accuracy, (E_{total})

images before RBC generation, the retrieval error for all three methods was 541.47. A limitation of the Radon Transform (RT) is that filtering out image pixels before transformation caused a resulting loss in accuracy/resolution, because of the integral nature of the transform. This limitation can be seen in Tables 4.4-4.6, because all the edge-detection pre-processing techniques resulted in the same RBC retrieval error, regardless of number of projection angles. We noted increasing the projection angles (n_p) used to generate the RBC did not correspond to a decrease in retrieval error; Which indicated that pre-processing images with Prewitt, Sobel, and Canny edge-detectors had a detrimental effect on the original RBC technique. Transforming edge-images using the RT meant that only the detected boundary/edge pixel intensities were being integrated to form the output projection vectors. Thus the RT output projections of edge-images did not fully capture the biological region present in X-ray images. Compounded with the fact that the RBC generation process thresholds the Radon projections (see Line 8 of Algorithm 2.3) resulted in barcodes containing little representative features.

	$RBC_{Regenerated}$		$RBC_{Prewitt}$	
n_p	L_{code}	E_{total}	L_{code}	E_{total}
4	196	514.76	196	541.47
8	392	477.34	392	541.47
16	784	466.89	784	541.47
32	1568	456.34	1568	541.47

Table 4.4: Effect of binarizing images with Prewitt edge detection on retrieval accuracy, (E_{total})

	$RBC_{Regenerated}$		RBC_{Sobel}	
n_p	L_{code}	E_{total}	L_{code}	E_{total}
4	196	514.76	196	541.47
8	392	477.34	392	541.47
16	784	466.89	784	541.47
32	1568	456.34	1568	541.47

Table 4.5: Effect of binarizing images with Sobel edge detection on retrieval accuracy, (E_{total})

Binarizing the images with edge detectors such as Prewitt, Sobel, and Canny before RBC generation increased retrieval error. However, Binarizing X-ray images with adaptive thresholding before RBC generation increased retrieval accuracy on average by 21.45 or 4.5 percent over the original method. Pre-processing X-ray images with adaptive thresholding reduced retrieval error for the RBC technique by increasing the relative intensity of the pixels before integration with the RT.

	$RBC_{Regenerated}$		RBC_{Canny}	
n_p	L_{code}	E_{total}	L_{code}	E_{total}
4	196	514.76	196	541.47
8	392	477.34	392	541.47
16	784	466.89	784	541.47
32	1568	456.34	1568	541.47

Table 4.6: Effect of binarizing images with Canny edge detection on retrieval accuracy, (E_{total})

	$RBC_{Regenerated}$		$RBC_{Prewitt}$		RBC_{Sobel}		RBC_{Canny}		$RBC_{Adap.Thresh}$	
n_p	L_{code}	E_{total}	L_{code}	E_{total}	L_{code}	E_{total}	L_{code}	E_{total}	L_{code}	E_{total}
4	196	514.76	196	541.47	196	541.47	196	541.47	196	486.49
8	392	477.34	392	541.47	392	541.47	392	541.47	392	457.97
16	784	466.89	784	541.47	784	541.47	784	541.47	784	441.84
32	1568	456.34	1568	541.47	1568	541.47	1568	541.47	1568	443.22

Table 4.7: Effect of binarization of input images with edge filters and thresholding on retrieval accuracy, (E_{total})

4.2 Radon Barcode Generation

Barcode generation from Radon projections is at the heart of the Radon Barcode (RBC) technique and offers two distinct advantages for Content Based Medical Image Retrieval (CBMIR) systems in particular. Barcodes are small binary feature vectors which are computationally efficient to compare, and generating them from Radon projections decreases retrieval error in comparison to other binary coding techniques [35]. In the following section we introduce novel barcoding techniques which were inspired by the RBC methodology (see Algorithm 2.3, and Figure 2.9).

4.2.1 Binary Coded Decimal Radon Barcodes

In the previous sub-section, we explored the effect which image binarization had on the Radon Barcode (RBC) retrieval error. Similarly, in RBC generation, the Radon Transform (RT) output projection vector is thresholded (Algorithm 2.3, Line 8) using the median of its non-zero components. In this sub-section, we investigate the effect which thresholding the Radon projections has on retrieval error. We propose using Binary Coded Decimal (BCD) and Gray Code (GC) to encode the output of Radon Transform (RT) in the RBC generation process to create Binary Coded Decimal Radon Barcodes (BCDRBC)s. We used Gray Code (GC) (using Algorithm 4.1) to reduce the bit entropy (number of changes between successive digits to reduce bit errors). Table 4.8 compares the BCDRBC to the RBC in terms of barcode length (L_{code}) and retrieval error (E_{Total}). Algorithm 4.1 outlines the process used to encode Binary Coded Decimal (BCD) strings using GC and Algorithm 4.2 describes how the BCDRBC is generated.

Algorithm 4.1 Gray Code Algorithm (GC)

```
1: Initialize Gray Code  $\mathbf{g} \leftarrow \emptyset$ 
2: Initialize Binary Code  $\mathbf{b} \leftarrow \mathbf{B}$ 
3:  $\mathbf{g}(1) \leftarrow \mathbf{b}(1)$ 
4: for  $i \leftarrow 2 : length(\mathbf{b})$  do
5:    $x \leftarrow xor(\mathbf{b}(i-1), \mathbf{b}(i))$ 
6:    $\mathbf{g}(i) \leftarrow x$ 
7: end for
8: end
9: Return  $\mathbf{g}$ 
```

GC is the process of encoding binary sequence to reduce the number of bit flips in a binary sequence, which reduces the probability of bit errors. Algorithm 4.1 shows the process used to encode a binary input sequence (\mathbf{B}) using GC. Line 1 and 2:

Initialize two arrays; One to store the GC output (line 1) and the other to store the input binary sequence (line 2). Line 3: Set the first element of the GC output array to the first bit of the binary input sequence. Line 4 to 7: Iteratively code the binary input array into GC by performing an exclusive OR operation between the i 'th and $i - 1$ elements of input binary sequence (line 5). Line 6: Store the result of the XOR operation into the i 'th element of the GC output array. Line 9: Return the output GC binary sequence stored in (\mathbf{g}) .

Algorithm 4.2 Binary Coded Decimal Radon Barcode Algorithm (BCDRBC)

```

1: Initialize Radon Barcode  $r \leftarrow \emptyset$ 
2: Initialize angle  $\theta \leftarrow 0$  and  $R_N = C_N \leftarrow 32$ 
3: Normalize the input image  $\bar{I} = \text{Normalize}(I, R_N, C_N)$ 
4: Set the number of projection angles, e.g.  $n_p \leftarrow 4$ 
5: Find the Radon projections:  $p_{i,\theta} = \text{Radon}(\bar{I}, \theta_{np})$ 
6: while  $\theta < 180$  do
7:   Get all projections  $\mathbf{p}$  for  $\theta$ 
8:   Convert all values to BCD16:  $\mathbf{b} \leftarrow \text{gray}(\text{BCD16}(\text{floor}(\mathbf{p})))$ 
9:   Append the new row  $\mathbf{r} \leftarrow \text{append}(\mathbf{r}, \mathbf{b})$ 
10:   $\theta \leftarrow \theta + \frac{180}{n_p}$ 
11: end while
12: end
13: Return  $\mathbf{r}$ 

```

The BCDRBC technique we propose improves the accuracy of the RBC by encoding entire RT projections as BCDs. Lines 1 and 2: Initialize the BCDRBC output (\mathbf{r}) as an empty array, $\theta = 0$, image row (R_N) and column size C_N to 32 pixels. Line 3: Normalize the X-ray image to R_N by C_N pixels. Line 4: Set the desired number of projection angles to find the RT. Line 5: Calculate the RT for the normalized X-ray image at the desired projection angles (θ_{np}) . Line 6 -11: Iteratively encode the output of the RT as GC BCDs. Lines 7 and 8: Store the entire Radon projection at angle θ into the empty array (\mathbf{p}) and converted each array element into an unsigned

16-bit GC BCD. BCD conversion begins with rounding a floating-point input value to an integer through the floor function. All the Radon projection vector elements are converted into their 16-bit unsigned binary representations, with a range of 0 to 65,536. If any projection values exceed the maximum or minimum of the unsigned a 16-bit binary number, they are replaced with that value. After BCD conversion each Radon projection value is then converted to GC using the process in Algorithm 4.1. Line 9: Append the GC BCD projections to the BCDRBC output array (\mathbf{r}). Line 13: Return the generated BCDRBC for the input X-ray image.

A notable reduction in retrieval error (E_{total}) between the BCDRBC and RBC approaches in favor of BCDRBC is shown in Table 4.8. The average drop in retrieval error was measured to be 116.68 or 24.36% between the two compared approaches, showing that encoding Radon projections as GC BCDs is effective in decreasing retrieval error. Table 4.8 also shows that the retrieval error also decreases as we increase the number of projection angles (n_p). However, barcode Lengths (L_{code}) shown in Table 4.8 were 16 times larger for BCDRBC when compared to RBC, because 16 bits were used to encode the Radon projection values. Although there is a significant increase in retrieval accuracy, the longer code length may prove to be a limiting factor during implementations of any potential CBMIR systems.

	$RBC_{Regenerated}$		$BCDRBC_{16}$	
n_p	L_{code}	E_{total}	L_{code}	E_{total}
4	196	514.76	3136	375.26
8	392	477.34	6272	360.28
16	784	466.89	11760	358.22
32	1568	456.34	25088	354.87

Table 4.8: RBC and BCDRBC retrieval accuracy (E_{total})

4.2.2 Difference of Radon Projections Barcodes

Babaie et al. investigated the effects of using single and orthogonal pair Radon projections to help reduce retrieval error in [3]. A follow-up study, introduced Local Radon Descriptor (LRD)s [2] which have been reported to decrease retrieval error by utilizing derivatives of Radon projections in small local image segments. Building upon the finding that differentiating the Radon Transform (RT) can help reduce retrieval error [3], we introduce Difference of Radon Projections Barcodes (DRPBC)s in Algorithm 4.3 which are Radon Barcode (RBC)s generated from the gradient of the RT.

Algorithm 4.3 Difference of Radon Projections Barcode Algorithm (DRPBC)

- 1: Initialize Difference of Radon Projections Barcode $r \leftarrow \emptyset$
 - 2: Initialize angle $\theta \leftarrow 0$ and $R_N = C_N \leftarrow 32$
 - 3: Normalize the input image $\bar{I} = \text{Normalize}(I, R_N, C_N)$
 - 4: Set the number of projection angles, e.g. $n_p \leftarrow 4$
 - 5: Find the Radon projections: $p_{i,\theta} = \text{Radon}(\bar{I}, \theta_{np})$
 - 6: Find the Gradient of the Radon Projections: $\mathbf{G}_{i,\theta} = \text{gradient}(p_{i,\theta})$ using Equations 2.13, 2.17, and 2.18.
 - 7: **while** $\theta < 180$ **do**
 - 8: Get the magnitude of all gradient values $|\mathbf{G}_i|$ for θ
 - 9: Find typical values: $T_{\text{typical}} \leftarrow \text{median}(|\mathbf{G}_i|)_{|\mathbf{G}_i| \neq 0}$
 - 10: Threshold projections: $\mathbf{b} \leftarrow |\mathbf{G}_i| \geq T_{\text{typical}}$
 - 11: Append the new row $\mathbf{r} \leftarrow \text{append}(\mathbf{r}, \mathbf{b})$
 - 12: $\theta \leftarrow \theta + \frac{180}{n_p}$
 - 13: **end while**
 - 14: **end**
 - 15: Return \mathbf{r}
-

Similar to the RBC, DRPBCs are created by binarizing output projections of the spatial gradient of the RT. The spatial gradient of the RT is calculated by convolving the Sobel kernel (Figure 2.5) with the RT projection matrix as described in Algorithm 4.3. Line 1 and 2: Initialize empty DRPBC output array, $\theta = 0$, and set the image row and column size to 32. Line 3 and 4: Resize the image to the image row and

column size, and set the number of projections used to calculate the RT. Line 5 and 6: Find the RT of the image and then calculate the spatial gradient of the RT matrix by convolving with the Sobel kernel (Figure 2.5). Line 8: Find the magnitude of all the gradient values of the RT at angle θ , by finding the corresponding column of the gradient. Line 9: Find the median of the non-zero elements of the gradient and store that as the threshold value ($T_{typical}$). Line 10: Threshold the Gradient values using the calculated threshold value ($T_{typical}$) and store them into a temporary array, **b**. Line 11: Append the binarized gradient value for the θ value being processed in the output barcode array (**r**). Line 12 to 14: Iterate θ according to the maximum number of desired projections (n_p). Line 15: Return the DRPBC for the image being processed.

	<i>RBC_{Regenerated}</i>		DRPBC	
n_p	L_{code}	E_{total}	L_{code}	E_{total}
4	196	514.76	196	417.16
8	392	477.34	392	347.70
16	784	466.89	784	310.74
32	1568	456.34	1568	303.40

Table 4.9: RBC and DRPBC retrieval accuracy (E_{total})

As shown in Table 4.9, the DRPBC has a considerably lower retrieval error (E_{total}) than the RBC (on average 134 or by 28%) while maintaining the same barcode length. We postulate that the decrease in retrieval error occurs because the spatial gradient of the RT encodes changes between Radon projections at different projection angles. The generated DRPBC encodes more information relating to the shape and structure of its originating image and improving CBMIR performance. Although we used the Sobel method (see Section 2.1.2) for calculating the gradient of the RT in Algorithm 4.3. Calculating the image gradient with the Prewitt operator had a similar effect,

albeit with higher retrieval error. The decrease in retrieval error we observed suggests that barcoding the differences between different Radon projections contained more representative image information than the projections alone.

4.2.3 Soft Radon Hash Barcodes

Lefebvre et al. proposed Radon Soft Hash (RASH) [19] [18] to identify attacks or alterations to images based the middle points of an image’s Radon projections. Reasoning that the middle point (P_{middle}) of each Radon projection vector encoded unique information about an image while being relatively rotation and scale-invariant. The Radon Soft Hash (RASH) descriptor was attractive to Content Based Medical Image Retrieval (CBMIR) applications because it had the potential to reduce barcode size in comparison to other Radon Barcode (RBC) methods. We applied the RASH methodology to reduce the length (L_{code}) of generated Difference of Radon Projections Barcodes (DRPBC)s while maintaining a similar retrieval error (E_{Total}).

$$P_{middle} = floor \left(\sqrt{\frac{width^2 + height^2}{2}} \right) \quad (4.1)$$

Lefebvre et al. proposed Equation 4.1 in [19] to find the middle points of the Radon Transform (RT) projections from image height and width. The RT is calculated from the origin or middle of the image (see Figure 4.2), which usually contains the majority of image content. Thus middle points of the RT are the most scale and rotation invariant points in the entire transform. X-ray images were centered upon the patient because the detector area was on average smaller than the subject being imaged. Instead of using only the middle points of the RT, we consider a region around

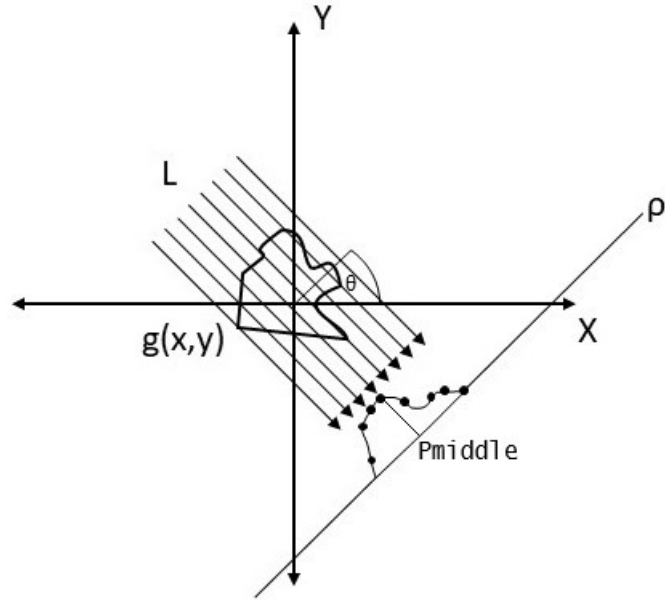


Figure 4.2: Graphical illustration for RASH

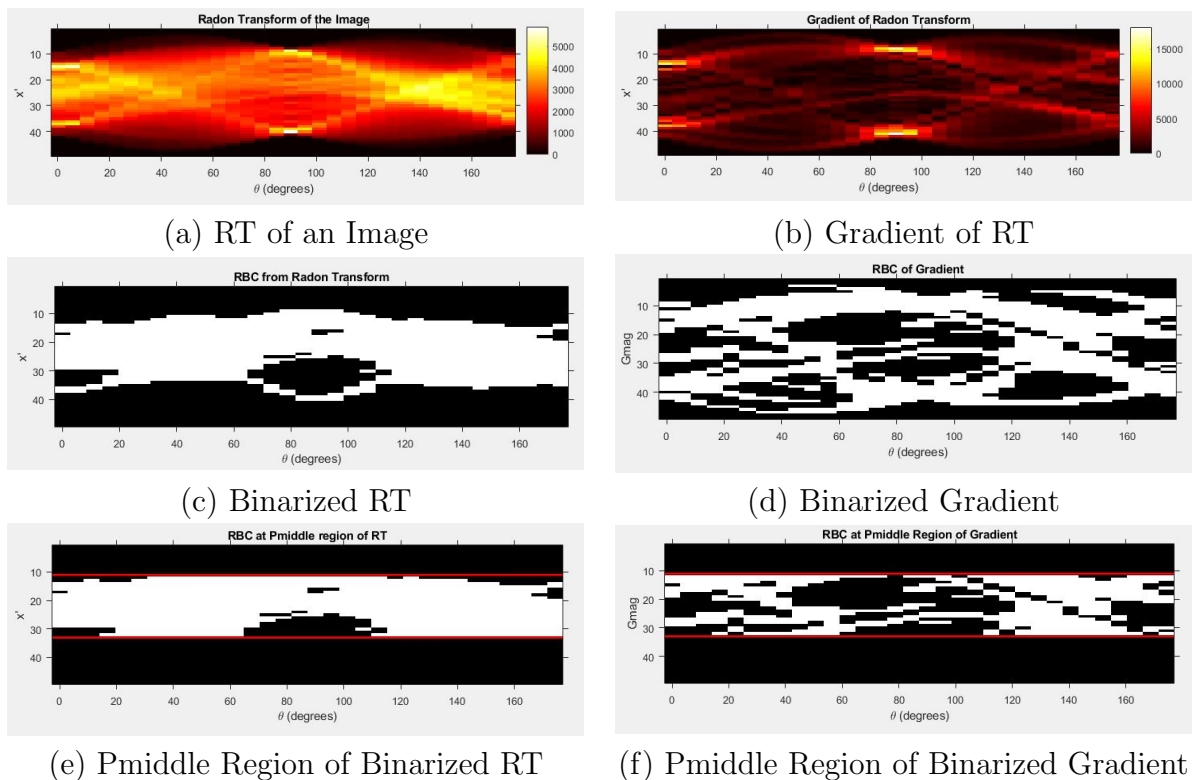


Figure 4.3: Segmentation of Pmiddle Region from the RT and the Gradient

them to encode more representative binary features (see Figure 4.3 (e)-(f)). Encoding only the region around the middle points helped decrease retrieval error while keeping the barcode length relatively small. Figure 4.3 shows a comparison between encoding the middle region of the traditional RBC approach and the DRPBC introduced in the previous section.

Algorithm 4.4 Difference of Radon Projection Soft Hash Barcode Algorithm (DRP-SHBC)

- 1: Initialize Soft Radon Hash Barcode $r \leftarrow \emptyset$
 - 2: Initialize angle $\theta \leftarrow 0$ and $R_N = C_N \leftarrow 32$
 - 3: Normalize the input image $\bar{I} = \text{Normalize}(I, R_N, C_N)$
 - 4: Set the number of projection angles, e.g. $n_p \leftarrow 4$
 - 5: Find the Radon projections: $p_{i,\theta} = \text{Radon}(\bar{I}, \theta_{np})$
 - 6: Find the Gradient of the Radon Projections: $\mathbf{G}_{i,\theta} = \text{gradient}(p_{i,\theta})$ using Equations 2.13, 2.17, and 2.18
 - 7: Calculate middle points: $P_{middle} \leftarrow fl\left(\sqrt{\frac{width^2 + height^2}{2}}\right)$
 - 8: **while** $\theta < 180$ **do**
 - 9: Get the magnitude of all gradient values $|\mathbf{G}_i|$ for θ
 - 10: Find typical values: $T_{typical} \leftarrow \text{median}(|\mathbf{G}_i|)_{|\mathbf{G}_i| \neq 0}$
 - 11: Find all the middle projection points: $|\mathbf{G}_i| \leftarrow |\mathbf{G}_i|(fl(\frac{P_{middle}}{2}) : fl(\frac{3P_{middle}}{2}))$
 - 12: Threshold projections: $\mathbf{b} \leftarrow |\mathbf{G}_i| \geq T_{typical}$
 - 13: Append the new row $\mathbf{r} \leftarrow \text{append}(\mathbf{r}, \mathbf{b})$
 - 14: $\theta \leftarrow \theta + \frac{180}{n_p}$
 - 15: **end while**
 - 16: **end**
 - 17: Return \mathbf{r}
-

Similar to the other RBC approaches generating Difference of Radon Projections Soft Hash Barcode (DRPSHBC) begins with first normalizing the image finding the RT, gradient of the RT, and creating a barcode from middle regions binarized gradient as described in Algorithm 4.4. Line 1 and 2: Initialize empty DRPBC output array, $\theta = 0$, and set the image row and column size to 32. Line 3 and 4: Resize the image to the image row and column size, and set the number of projections used to calculate the RT. Line 5 and 6: Find the RT of the image and then calculate

the spatial gradient of the RT matrix by convolving with the Sobel kernel (Figure 2.5). Line 7: Calculate the middle points (P_{middle}) for the RT. Line 9: Find the magnitude of all the gradient values ($|G_i|$) of the RT at angle θ . Line 10: Find the median of the non-zero elements of the gradient and store that as the threshold value ($T_{typical}$). Line 11: Truncate the gradient to only the middle region defined by $\frac{P_{middle}}{2}$ and $\frac{3P_{middle}}{2}$. Line 12: Threshold the truncated middle gradient values using the calculated threshold value ($T_{typical}$) and store them into a temporary array, \mathbf{b} . Line 13: Append the binarized gradient value for the θ value being processed in the output barcode array (\mathbf{r}). Line 14 to 16: Iterate θ according to the maximum number of desired projections (n_p). Line 15: Return the DRPSHBC for the image being processed.

	$RBC_{Regenerated}$		DRPSHBC	
n_p	L_{code}	E_{total}	L_{code}	E_{total}
4	196	514.76	92	476.88
8	392	477.34	184	383.39
16	784	466.89	368	333.53
32	1568	456.34	736	332.00

Table 4.10: RBC and RSHDRPBC retrieval accuracy (E_{total})

Table 4.10 shows the effect encoding the region around the middle points for the DRPSHBC, and highlights the reduction in barcode length associated with it. The barcode length of the DRPSHBC was on average less than half the size of the RBC length, while retrieval error was decreased by 100 or 20% on average. Comparing the results of the DRPBC, to the DRPSHBC, we saw that only encoding the middle regions of the gradient did lead to information loss because the retrieval error increased by 10-20 in the DRPSHBC. We observed a correlation between increasing the number of projection angles and retrieval error because encoding more information led to a smaller retrieval error. Table 4.10 shows that the DRPSHBC (Algorithm 4.4) had

significantly better performance than the RBC in terms of retrieval error and barcode length, and are quite possibly one of the best global binary barcoding technique for CBMIR applications.

4.3 Distance Measures

In Section 3.2 two binary distance measures were introduced, Hamming Distance (HD) and the Binary Euclidean Distance (BED). HD was used in the original Radon Barcode (RBC) technique [35] and Binary Euclidean Distance (BED) was introduced in [10] as an alternative distance metric for comparing binary vectors. Table 4.11

	RBC_{HD}		RBC_{BED}	
n_p	L_{code}	E_{total}	L_{code}	E_{total}
4	196	514.76	196	518.12
8	392	477.34	392	474.22
16	784	466.89	784	461.40
32	1568	456.34	1568	451.87

Table 4.11: Effect of different distance measures, HD and BED on RBC retrieval accuracy (E_{total})

compares the two distance measures in terms of retrieval error (E_{total}). BED was measured to have a lower retrieval error for longer length barcodes ($np > 8$), whereas HD appears to work better for smaller barcodes. The slight variation of both distance measures with increasing barcode length is indicative of each measures invariance to increasing sparsity. Although using BED as a distance measure increases retrieval accuracy, the relative difference between using BED and HD is minimal in comparison to the other factors investigated in the above sections.

Chapter 5

Conclusions and Future Work

5.1 Conclusions

Content Based Medical Image Retrieval (CBMIR) systems have shown to be an invaluable tool for medical databases and information systems. Complementary feature vectors such as the Radon Barcode (RBC) are critical to the efficient and accurate retrieval phase of CBMIR systems. RBCs can be used in the preliminary search phase of CBMIR systems to quickly shortlist candidate solutions in preparation for advanced and precise techniques to match images. RBC based techniques, like all binary similarity measures, encode vast amounts of image information in relatively short binary codes. This work introduced several novel optimizations in terms of image pre-processing, barcode generation, and distance evaluation techniques which improve the effectiveness of RBCs as complementary feature vectors in CBMIR systems. In Section 4 optimizations to image processing, barcode generation, and binary vector distance measures were proposed and compared to the RBC process and the Image Retrieval Medical Application (IRMA) dataset. After comparison to the RBC technique from [35], it was found that the optimizations we proposed decreased re-

trieval error (E_{Total}), barcode length (L_{code}), or both.

In Section 4.1, different medical image pre-processing techniques like histogram equalization and image binarization were investigated for their effect of RBC retrieval error. Applying histogram equalization to images from the IRMA dataset tended to reduce the retrieval error by removing intensity variations in source images. Binarizing using adaptive thresholding decreased the retrieval error by increasing the data available for the RBC to encode. However, this effect of adaptive thresholding diminished as the number of projection angles (n_p) encoded increased, suggesting that binarization process improved the capability of the RBC to better encode border information about objects in the image. Image binarization using edge-detection kernels such as the Prewitt, Sobel, and Canny operators introduced in Section 2.1.2 increased retrieval error to a seemingly fixed value. A possible cause for all three edge-detection techniques generating RBCs which all had the same retrieval error is the integral nature of the Radon Transform (RT). The RT only considers the integration of intensity values onto the ρ axes at different projection angles, and reducing the amount of the integrated pixels caused significant losses in resolution for the Radon projections. Pre-processing images with techniques like histogram equalization, and adaptive thresholding reduce RBC retrieval error by normalizing inter-image intensities and amplifying representation of object boundaries in generated barcodes.

In Section 4.2 we proposed several novel binary barcoding techniques based off of the RBC such as the Binary Coded Decimal Radon Barcodes (BCDRBC), Difference of Radon Projections Barcodes (DRPBC), and Difference of Radon Projections Soft Hash Barcode (DRPSHBC). The BCDRBC introduced in Section 4.2.1 encoded the numerical values of the RT projections into 16-bit Binary Coded Decimal (BCD),

to prevent information loss from thresholding. BCDRBC retrieval error was significantly lower (by 24% on average) than the conventional RBC technique, but the resulting barcode was 16 times longer (16-bit encoding). Section 4.2.2 introduced the DRPBC which applied the conventional RBC technique to the gradient of the RT. DRPBC retrieval error rates were lower (by 28% on average) than any other technique which we tested while maintaining the same barcode length as the conventional RBC. Barcoding the gradient of the RT significantly improved the retrieval error of the RBC process because the gradient allowed for the encoding of inter-projection intensity variations. Information relating to the differences or variations between Radon projections at different angles is representative of the boundary shape of the object undergoing the RT. DRPSHBC, introduced in Section 4.2.3 were based upon the DRPBC, but reduced the barcode size by only encoding the middle region of the gradient of the RT. The resulting DRPSHBC had less than half the barcode length of DRPBCs but had only a slightly higher retrieval error (10% on average). DRPSHBC had the second-lowest retrieval error and the smallest barcode length out of all the barcoding techniques tested. DRPSHBC have the lowest barcode length and the DRPBC had the lowest retrieval error from all the techniques tested in Section 4.2.

In Section 4.3 changing distance metric used for determining binary vector distance from HD to BED in a minute decrease in RBC retrieval error (%0.5). The resulting difference in retrieval error between using HD or BED for RBC binary vector comparison didn't appear to have a noticeable difference. Although the distance measure did not have a significant impact on the retrieval error of the RBC, we found that having the flexibility to choose the distance measure helps in developing CBMIR systems.

This study outlined several key optimizations to improve the RBC generation

process, such as image pre-processing, barcode formation, and distance metrics. We compared each proposed optimization to the RBC method quantitatively based on retrieval error and barcode length to determine its efficacy. In Section 4.2.2 we proposed, DRPBC, a barcode generation scheme which to our knowledge outperformed all other global barcoding techniques in terms of retrieval error (see Table 2.2 and 4.9). In section 4.2.3 we introduced, DRPSHBCs which are a global barcoding technique, which to our knowledge have both the smallest barcode size and retrieval error. The optimal barcoding technique for use as a complementary feature for CBMIR applications is DRPSHBC because of its small retrieval error and barcode length.

5.2 Summary of Contributions

Throughout this study, we investigated ways to improve the Radon Barcode (RBC) technique as a complementary feature in Content Based Medical Image Retrieval (CBMIR) systems. We introduced several novel techniques and optimizations which improve retrieval error and reduce barcode length, such as:

- Pre-processing images with histogram equalization or adaptive thresholding reduced retrieval error.
- Encoding the Radon Transform (RT) using Binary Coded Decimal (BCD) techniques such as the Binary Coded Decimal Radon Barcodes (BCDRBC) reduced retrieval error at the expense of barcode length.
- Using the gradient of the RT to generate barcodes similar to the Difference of Radon Projections Barcodes (DRPBC) significantly reduced retrieval error while perserving barcode length.

- Encoding middle regions of gradient of the RT like the Difference of Radon Projections Soft Hash Barcode (DRPSHBC) significantly reduces barcode length while giving similar retrieval accuracies.
- Performing binary match evaluations using Binary Euclidean Distance (BED) instead of Hamming Distance (HD) gives a lower retrieval error.

5.3 Future Research Direction

In future research on optimizing the RBC technique, we aim to explore different barcoding techniques which take advantage of the integral nature of the RT and inter-projection differences like the proposed gradient-based approaches. Though the results which we proposed were promising, all tests needed to be conducted independently because each proposed technique/optimization technique changed the effectiveness of the following downstream methods. We hope to computationally find the optimal combination of pre-processing, barcode formation, and binary evaluation techniques for CBMIR applications which lower retrieval error and barcode length. Another area which we would like to investigate further is the relationship between retrieval error and the number of Radon projection angles. Increasing the projection angles does not always correspond to a decrease in retrieval error, and investigating the cause could lead to significant improvements in the RBC barcode generation process.

Bibliography

- [1] ADLAKHA, D., ADLAKHA, D., AND TANWAR, R. Analytical comparison between sobel and prewitt edge detection techniques. *International Journal of Scientific & Engineering Research* (2016).
- [2] BABAIE, M., TIZHOOSH, H. R., KHATAMI, A., AND SHIRI, M. Local radon descriptors for image search. In *2017 Seventh International Conference on Image Processing Theory, Tools and Applications (IPTA)* (2017), IEEE, pp. 1–5.
- [3] BABAIE, M., TIZHOOSH, H. R., ZHU, S., AND SHIRI, M. Retrieving similar x-ray images from big image data using radon barcodes with single projections. *arXiv preprint arXiv:1701.00449* (2017).
- [4] BANKMAN, I. *Handbook of medical image processing and analysis*. Elsevier, 2008.
- [5] BRACEWELL, R. N. Two-dimensional signal processing and imaging. *New Jersey* (1995), 518–525.
- [6] BRADLEY, D., AND ROTH, G. Adaptive thresholding using the integral image. *Journal of graphics tools* 12, 2 (2007), 13–21.

- [7] BRADY, A., LAOIDE, R. Ó., MCCARTHY, P., AND MCDERMOTT, R. Discrepancy and error in radiology: concepts, causes and consequences. *The Ulster medical journal* 81, 1 (2012), 3.
- [8] CANNY, J. A computational approach to edge detection. *IEEE Transactions on pattern analysis and machine intelligence*, 6 (1986), 679–698.
- [9] CANNY, J. A computational approach to edge detection. In *Readings in computer vision*. Elsevier, 1987, pp. 184–203.
- [10] CHOI, S.-S., CHA, S.-H., AND TAPPERT, C. C. A survey of binary similarity and distance measures. *Journal of Systemics, Cybernetics and Informatics* 8, 1 (2010), 43–48.
- [11] CUI, S., WANG, Y., QIAN, X., AND DENG, Z. Image processing techniques in shockwave detection and modeling. *Journal of Signal and Information Processing* 4, 03 (2013), 109.
- [12] DEBNATH, L., AND BHATTA, D. *Integral transforms and their applications*. Chapman and Hall/CRC, 2006.
- [13] ERFANKHAH, H., YAZDI, M., AND TIZHOOSH, H. R. Combining real-valued and binary gabor-radon features for classification and search in medical imaging archives. In *2017 IEEE Symposium Series on Computational Intelligence (SSCI)* (2017), IEEE, pp. 1–5.
- [14] FRANK, G. Pulse code communication, 1953. US Patent 2,632,058.
- [15] GONZALEZ, R. C., AND WOODS, R. E. Histogram processing. *Digital Image Processing* 3 (2008), 162–165.
- [16] GREEN, B. Canny edge detection tutorial. *Retrieved: March 6 (2002), 2005*.

- [17] KHATAMI, A., BABAIE, M., TIZHOOSH, H. R., KHOSRAVI, A., NGUYEN, T., AND NAHAVANDI, S. A sequential search-space shrinking using cnn transfer learning and a radon projection pool for medical image retrieval. *Expert Systems with Applications* 100 (2018), 224–233.
- [18] LEFEBVRE, F., CZYZ, J., AND MACQ, B. M. A robust soft hash algorithm for digital image signature. In *ICIP (2)* (2003), pp. 495–498.
- [19] LEFEBVRE, F., MACQ, B., AND LEGAT, J.-D. Rash: Radon soft hash algorithm. In *Signal Processing Conference, 2002 11th European* (2002), IEEE, pp. 1–4.
- [20] LEHMANN, T., DESELAERS, T., SCHUBERT, H., GÜLD, M. O., THIES, C., FISCHER, B., AND SPITZER, K. A content-based approach to image retrieval in medical applications. *Emerging Trends and Challenges in IT Management. Achen University of Technology* (2006), 118–32.
- [21] LIU, X., TIZHOOSH, H. R., AND KOFMAN, J. Generating binary tags for fast medical image retrieval based on convolutional nets and radon transform. In *Neural Networks (IJCNN), 2016 International Joint Conference on* (2016), IEEE, pp. 2872–2878.
- [22] MAINI, R., AND AGGARWAL, H. Study and comparison of various image edge detection techniques. *International journal of image processing (IJIP)* 3, 1 (2009), 1–11.
- [23] MLLER, H., CLOUGH, P., DESELAERS, T., AND CAPUTO, B. Image-clef: Experimental evaluation in visual information retrieval series. *The information retrieval series, Springer* (2010).

- [24] NOUREDANESH, M., TIZHOOSH, H. R., AND BANIJAMALI, E. Gabor barcodes for medical image retrieval. In *Image Processing (ICIP), 2016 IEEE International Conference on* (2016), IEEE, pp. 2490–2493.
- [25] NOUREDANESH, M., TIZHOOSH, H. R., BANIJAMALI, E., AND TUNG, J. Radon-gabor barcodes for medical image retrieval. In *Pattern Recognition (ICPR), 2016 23rd International Conference on* (2016), IEEE, pp. 1309–1314.
- [26] OTSU, N. A threshold selection method from gray-level histograms. *IEEE transactions on systems, man, and cybernetics* 9, 1 (1979), 62–66.
- [27] PREWITT, J. M. Object enhancement and extraction. *Picture processing and Psychopictorics* 10, 1 (1970), 15–19.
- [28] PRINCE, J. L., AND LINKS, J. M. *Medical imaging signals and systems*. Pearson Prentice Hall Upper Saddle River, NJ, 2006.
- [29] RAHNAMAYAN, S., AND TIZHOOSH, H. R. Image thresholding using micro opposition-based differential evolution (micro-ode). In *Evolutionary Computation, 2008. CEC 2008. (IEEE World Congress on Computational Intelligence). IEEE Congress on* (2008), IEEE, pp. 1409–1416.
- [30] ROGERS, W., RYACK, B., AND MOELLER, G. Computer-aided medical diagnosis: literature review. *International journal of bio-medical computing* 10, 4 (1979), 267–289.
- [31] RUSS, J., AND NEAL, F. Image enhancement in the spatial domain. *The Image Processing Handbook* (2011), 269–336.
- [32] SOBEL, I. An isotropic 3×3 image gradient operator. *Machine vision for three-dimensional scenes* (1990), 376–379.

- [33] SRIRAM, A., KALRA, S., TIZHOOSH, H. R., AND RAHNAMEYAN, S. Learning autoencoded radon projections. In *2017 IEEE Symposium Series on Computational Intelligence (SSCI)* (2017), IEEE, pp. 1–5.
- [34] SZE-TO, A., TIZHOOSH, H. R., AND WONG, A. K. Binary codes for tagging x-ray images via deep de-noising autoencoders. In *Neural Networks (IJCNN), 2016 International Joint Conference on* (2016), IEEE, pp. 2864–2871.
- [35] TIZHOOSH, H. R. Barcode annotations for medical image retrieval: A preliminary investigation. In *Image Processing (ICIP), 2015 IEEE International Conference on* (2015), IEEE, pp. 818–822.
- [36] TIZHOOSH, H. R., GANGEH, M. J., TADAYYON, H., AND CZARNOTA, G. J. Tumour roi estimation in ultrasound images via radon barcodes in patients with locally advanced breast cancer. *arXiv preprint arXiv:1602.02586* (2016).
- [37] TIZHOOSH, H. R., MITCHELTREE, C., ZHU, S., AND DUTTA, S. Barcodes for medical image retrieval using autoencoded radon transform. *arXiv preprint arXiv:1609.05112* (2016).
- [38] TIZHOOSH, H. R., AND RAHNAMEYAN, S. Evolutionary projection selection for radon barcodes. In *Evolutionary Computation (CEC), 2016 IEEE Congress on* (2016), IEEE, pp. 1–8.
- [39] TIZHOOSH, H. R., ZHU, S., LO, H., CHAUDHARI, V., AND MEHDI, T. Min-max radon barcodes for medical image retrieval. In *International Symposium on Visual Computing* (2016), Springer, pp. 617–627.
- [40] VIOLA, P., AND JONES, M. J. Robust real-time face detection. *International journal of computer vision* 57, 2 (2004), 137–154.

- [41] WEI, C.-H. *Machine Learning Techniques for Adaptive Multimedia Retrieval: Technologies Applications and Perspectives: Technologies Applications and Perspectives*. IGI Global, 2010.
- [42] ZHU, S., AND TIZHOOSH, H. R. Radon features and barcodes for medical image retrieval via svm. *arXiv preprint arXiv:1604.04675* (2016).